



Università degli Studi di Napoli Federico II

Scuola Politecnica e delle Scienze di Base

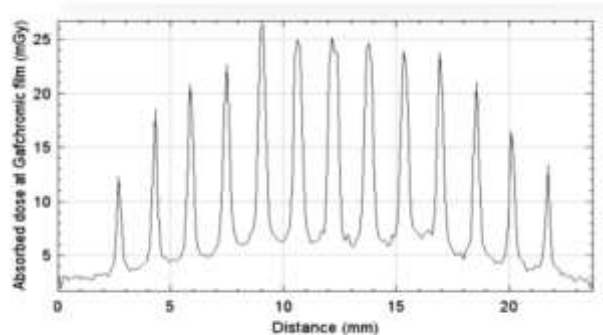
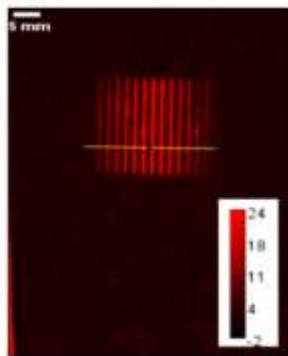
Collegio di Scienze

Dipartimento di Fisica "Ettore Pancini"

Corso di Laurea Magistrale in Fisica

TESI DI LAUREA SPERIMENTALE IN FISICA MEDICA

***Planar and rotational minibeam radiation therapy
for preclinical research: Monte Carlo simulations
with new collimators***



Relatori

Prof. Paolo Russo

Prof. Giovanni Mettivier

Dr. Antonio Sarno

Candidata

Dott.ssa Rita Camilla Buono

matr. N94000795

Anno Accademico 2022/2023

Table of contents

Introduction	3
Chapter 1: Minibeam Radiation Therapy	6
1.1 Peak to Valley Dose Rate and Percentage Depth Dose	12
1.2 Radiobiology.....	13
1.3 Recent developments	15
Chapter 2: Monte Carlo simulations.....	18
2.1 TOol of PArticles Simulation (TOPAS)	18
2.2 Simulation set-up	23
2.2.1 Collimator	25
2.2.2 Energy scoring.....	27
2.2.3 Phantom	27
2.3 Simulation results.....	29
2.3.1 MBRT lead collimator	29
2.3.2 MBRT brass collimator.....	32
2.4 Rotational MBRT	44
Chapter 3: Experimental validation.....	47
3.1 Measurement with 150 kVp source	47
3.2 Simulation with 150 kVp source	57
Conclusions.....	60
References	62
Acknowledgments.....	64

*To myself, to my determination,
to my dreams, to my emotionality,
to my rebirth.*

Introduction

Conventional broad beam radiotherapy is a highly effective radiotherapy technique commonly used in the treatment of tumours in the clinic. A new concept of external beam radiotherapy was investigated in the last few decades, which exploits spatially fractionated beams (spatially fractionated radiation therapy, SFRT). In SFRT the radiation beam is split into various beamlets, at variance with broad beam irradiation typically used for radiotherapy of solid tumours. SFRT originated from pre-clinical experiments at synchrotron radiation beamlines, where the high brilliance of the X-ray source, and suitable beam-shaping collimators, permitted to produce a series of beamlets with about 50 μm width, spaced about 500 μm apart (microbeam radiation therapy, MRT). MRT showed evidence of high-dose radiotherapy with high toxicity to the tumour cells and high tolerance of surrounding normal tissues, with specific interest for treating radioresistant brain tumours. The normal tissue sparing phenomenon observed in MRT with small animal models is still not fully understood and subject to intense research.

In this thesis I will deal with the minibeam radiation therapy (MBRT) technique. The MBRT technique consists in fractionating the beam spatially, generated by an orthovoltage X-ray tube, a clinically viable solution with respect to synchrotron radiation available only in few large facilities. In MBRT beamlets having a transverse width in the order of hundreds of micrometres (200-600 μm) are produced by suitably shaped metal collimators (e.g., in the form of comb, slit, pinhole or mesh collimators). In pre-clinical (animal) experiments, MBRT proved to spare the normal tissue traversed prior to the tumour and at the same time maintains tumour control equal to conventional radiation therapy.

The aim of the project "Developing and Optimizing X-Rays mini-beam Radiotherapy", promoted by the San Raffaele Hospital (HSR), Milan, in collaboration with the Azienda Ospedaliera Universitaria Federico II (AOU) and

Università Federico II of Naples, is to develop, optimize, verify dosimetry, and implement the MBRT technique for irradiation on small animals through the Small Animal Irradiator (SmArt), already present on site. This project was approved by the “Piano Nazionale di Ripresa e Resilienza” (PNRR) and funds (800 kEur) were allocated for this research, which started on 22 May 2023 (Project code: PNRR-POC-2022-12376062). The project consists of 3 different phases:

1. Collimators development, optimization, and dosimetry for MBRT. In particular, the impact of beam width and beam distance along with other physical characteristics (e.g., materials geometry etc.) will be investigated.
2. The performed MC simulation will be based on the GEANT4 toolkit and will provide 3D maps of absorbed dose in the tissues irradiated from one or multiple angles.
3. Cells and animal model experiments will be carried out to measure the biological effects for different collimator systems and irradiation geometries.

This thesis was carried out within the PNRR-Proof-of-Concept project (framework, PNRR-Sanità) led by HSR, for evaluating and validating the MBRT technique, through Monte Carlo simulations and pre-clinical experiments, including the realization of new collimator and irradiation strategies. Specifically, in this thesis I carried out the first Monte Carlo simulation for dosimetry assessment (in collaboration with HSR Milan) and realized new MBRT collimators.

This thesis consists of a first chapter in which the MB radiotherapy technique is presented, reporting scientific articles that experimentally demonstrate the validity of this technique, and describing the relevant radiobiological effects. The second chapter describes the Monte Carlo simulations with particular attention to the program involved for the simulations of the thesis, i.e., TOol of Particles Simulation (TOPAS); in addition, are presented the main features of the

simulations implemented with the TOPAS toolkit and the results obtained from these. In the third and final chapter is described the experimental system used and is analysed the results obtained from the experiment conducted in the laboratory of Federico II aimed at validating, albeit partially, the results obtained through the Monte Carlo simulations. The Conclusions follow.

Chapter 1: Minibeam Radiation Therapy

Radiotherapy is the most common technique used for the treatment of most types of existent tumours. The main concept behind conventional radiotherapy is to treat the cancer employing broad X-ray beams produced by a clinical linear accelerator, that irradiate from a several directions the whole tumoral mass with toxic doses of radiation, restricting the dose delivery to surrounding healthy tissues to safe limits. However, when a tumour is highly radioresistant or near to a radiosensitive organ/tissue the conventional technique with broad beams may cause an increase in the neurotoxicity of the closely normal tissue.

The aim of the MINIBEAM project is to investigate a new type of radiotherapy which limits the negative effects of normal tissue and uses higher doses than the conventional ones. For this purpose, a radiotherapy technique involving spatial dose fractionation has been developed in the last years, so called *Minibeam Radiation Therapy* (MBRT).

MBRT is a radiotherapy strategy based on a method of spatial dose modulation which uses a series of narrow (submillimetre) parallel beams. This technique aims to improve the effectiveness of radiotherapy of cancers and, at the same time, to reduce possible risks to neighbouring healthy tissues, due to excessive absorbed dose. Ultimately, MBRT represents a method to spare normal tissue cells placed before the tumoral mass that receive the same dose as the tumoral cells in the conventional radiotherapy. However, dose tolerance of normal tissues remains a limiting factor in dose delivery of radiotherapy. This radiotherapy technique is a development of the previous *Microbeam Radiation Therapy* (MRT), which is implemented with synchrotron radiation and therefore not usable in the clinical setting. MRT has been investigated mainly at the National Synchrotron Light Source (NSLS), Brookhaven National Laboratory (BNL), at the European Synchrotron Radiation Facility (ESRF), Grenoble (France). This method has produced two unique effects in animal models. First, the MRT treatment is

exceptionally well tolerated by normal tissues including the central nervous system (CNS) at doses of up to several hundred Gy in a single fraction [1]. Secondly, it preferentially damages malignant tumours at very high doses, i.e., 150 to 625 Gy in-beam doses, while causing little or no damage to the surrounding normal tissue. This technique has been developed exploiting the spatial fractionation previously seen through micrometric parallel beams. Fractionation consists in using irradiation beams with width in the order of tens of μm (typically 60-80 μm): this calls for the use of very intense x-ray radiation sources as available at synchrotron radiation beamlines and, for this reason, to have a relevant dose to be irradiated it is necessary to use synchrotron light sources. In this way it is possible to use doses up to several hundred Gray per second in a single fraction maintaining good tolerability.

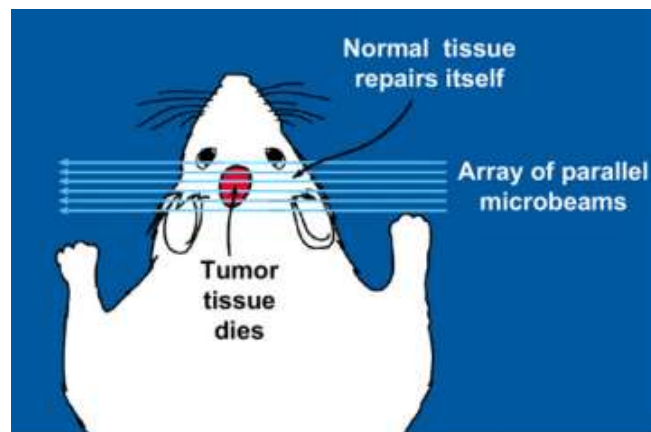


Figure 1: Schematic demonstration of microbeam radiation therapy idea [1].

Experimental evidence proved that using this spatial dose fractionation (MRT) technique on animals increases the tissue-sparing effect of healthy tissue. Thus, using submillimetre beamlets, it is possible to expand the irradiation area and, consequently, it is sufficient to have a source of lower X-ray flux such as produced by an X-ray tube.

MBRT is a promising example of how spatial dose modulation can lead to a net reduction in neurotoxicity while providing tumour control equivalent to or superior to the RT standard for high-grade gliomas. In fact, the therapeutic index

of radiotherapy (RT) treatments can be greatly improved by modifying dose delivery methods, such as temporal or spatial dose fragmentation.

The therapeutic index is closely linked to the concept of therapeutic window. The radiotherapy treatment plan must consider two fundamental factors: Tumour Control Probability (TCP) and Normal Tissue Complication Probability (NTCP). These are indicators of the control and therefore the treatment of the tumour and the complications that can develop in normal tissue, respectively. The goal of radiotherapy is to keep TCP high (>50%) and NTCP low (<5%), i.e. find a dose that allows these values to be obtained. Both curves representing the two examined parameters have sigmoidal trends (Figure 2), while the therapeutic window represents the distance between the two curves. It was proved that in the case of MBRT the two curves are more spaced and consequently the therapeutic window was better than conventional radiotherapy.

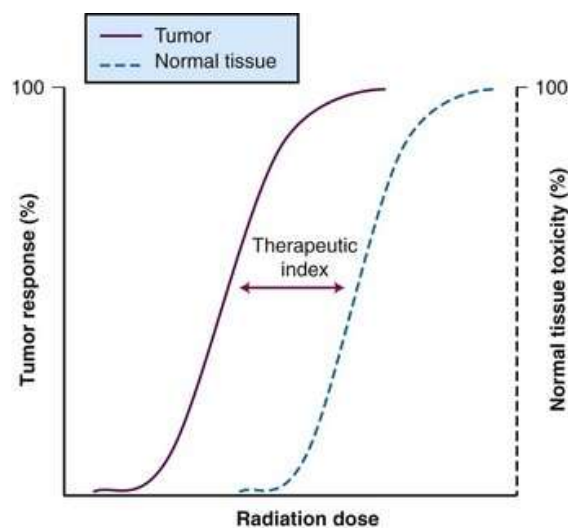


Figure 2: Sigmoid curves for TCP and NTCP reporting tumour response (%) and normal tissue toxicity (%) vs radiation dose.

Irradiation is carried out with one or more submillimetre beams (typically 400-700 μm) obtained by a collimator mounted at the bottom of the irradiation system. Generally, the collimator has one or more parallel slits but recently it has also been implemented with different configurations (e.g. divergent slits). The

previously used system source was the synchrotron, which allows to get doses around 100-200 Gy at the peak, while recently it has been developed with an orthovoltage X-ray tubes (225-320 kV tube voltage) for the treatment of tumour on small animals, obtaining an irradiation dose in the order of dozens of Grays. Currently, the technique is in the pre-clinical experimentation phase (irradiation on mice and/or rats) to verify its effectiveness and to determine the correct technological configuration. For this reason, the research group of Y. Prezado in 2017 found a way to adapt a pre-existent irradiation system, the Small Animal Research Platform (SARP), for the investigation of MBRT. The device consists of a specific collimator which is assembled at the bottom of the SARP (Figure 3) and which is characterised by a pattern with divergent beams to focus the region of interest. It was shown in this study the feasibility by means of a first in vivo experiment and the long-term effects by the follow up of the irradiated mice [2].

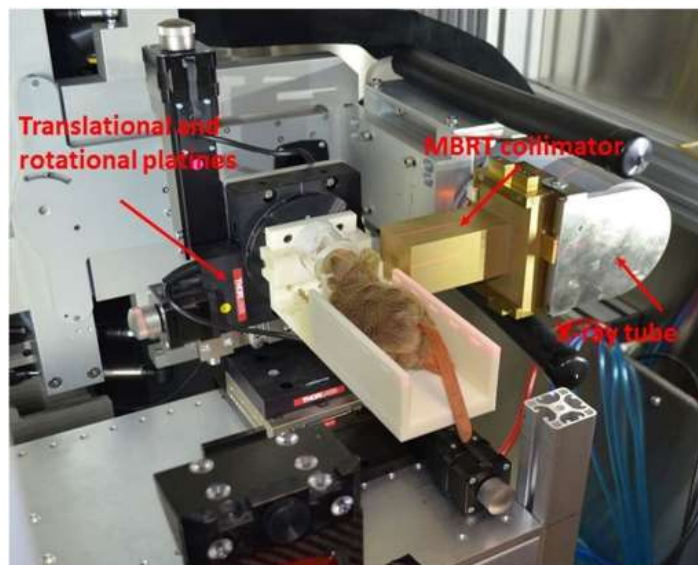


Figure 3: Configuration of the irradiation system for small animals [2].

Dose profiles consist of a succession of high-dose (*peak*) zones followed by low-dose areas (*valley*) (Figure 4), to preserve the normal cells in the valley and to give most of the dose to the tumoral cells in the peak.

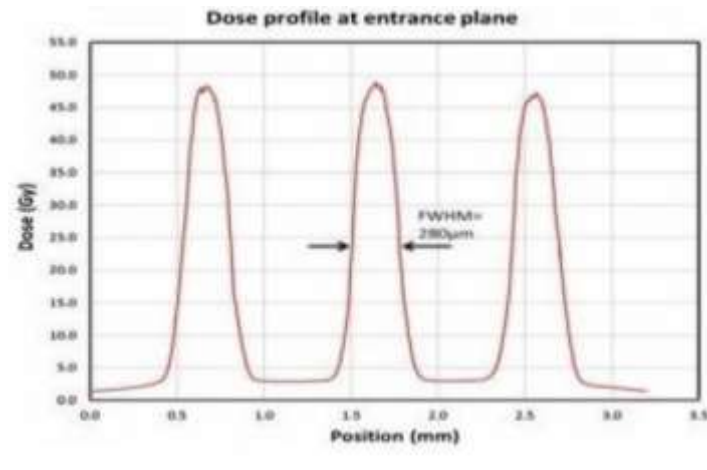


Figure 4: Surface dose profile of a phantom (2 cm × 2 cm) [3].

The main advantages of using MBRT are:

- Volume-dose effect, the lower the irradiated volume the greater the dose tolerated by the tissue. For this reason, having fractionated radiation beams allows to increase the dose in the peak, maintaining a great tolerance.
- The extension of the therapeutic window, as seen above, is a key factor in improving MBRT in comparison to conventional radiotherapy.
- The technological development is more straightforward than the MRT, but the biological effect of tissue sparing is maintained.
- MBRT effects feature the participation of different biological mechanisms if compared to conventional radiotherapy, which, however, are still unknown.

On the other hand, there are many cons that emerge by using this technique, such as:

- Dose rates are only relevant for close irradiation. Thus, in recent experiments on small animals the irradiation was done by positioning the target attached to the irradiation system. This place a considerable limitation in the clinical application of the mentioned radiotherapy since it is not possible to have the tumour close enough to the source.

- Currently used doses are not sufficiently managed by orthovoltage X-ray tube. Moreover, the dose rates actually gained are about dozens of Gy/min and the dose rates needed to treat a human tumour are about hundreds of Gy/min.
- Tolerance of normal tissues is not certain because the supposed doses that are employed for human irradiation are near the hundreds of Gy, possibly causing a negative effect on normal tissue.

MBRT presents many experimental evidences on its effectiveness. Recently, as shown in Figure 4, Sotiropoulos et al. (2021) discovered that the lifetime of rats irradiated by MBRT grew significantly, in comparison to the lifetime of rat irradiated by common radiotherapy (controls) [4]. The study compared the follow up of two groups of rats subjected to radiotherapy, both MBRT and BRT, to evaluate the effect of the different kinds of radiotherapy.

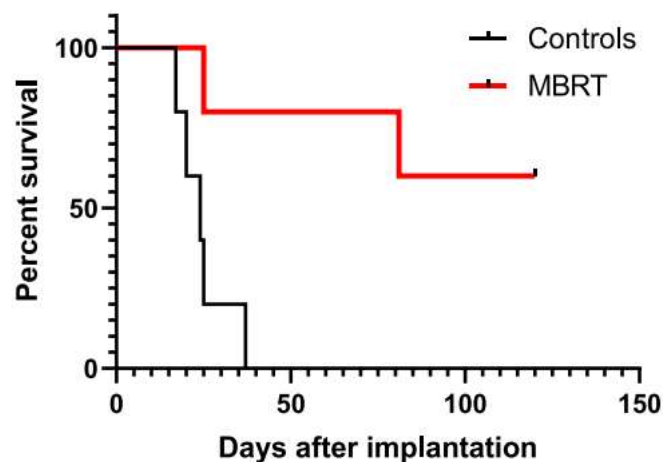


Figure 5: *Survival curves of the control and irradiated animals [4].*

Otherwise, the most challenging task is to estimate the delivered dose during a spatially fractionated RT treatment (i.e. MRT or MBRT both). For this reason, the study of K. M. Kraus (2022) for the first time would evaluate the MRT calculating the dose at a patient in different scenario using a Monte Carlo simulation 3D slicer [5]. They would prove the efficiency of spatially fractionated RT in tumour treatment both maintaining the same tumour control of conventional RT and

saving the normal tissue. Not only the PVDR is a parameter to take care of, but they also suggest using the equivalent uniform dose (EUD). The dosimetry results showed that MRT as comparable dose delivery method for most clinical scenarios investigated, keeping the irradiated volume at acceptable level (Figure 6) [5].

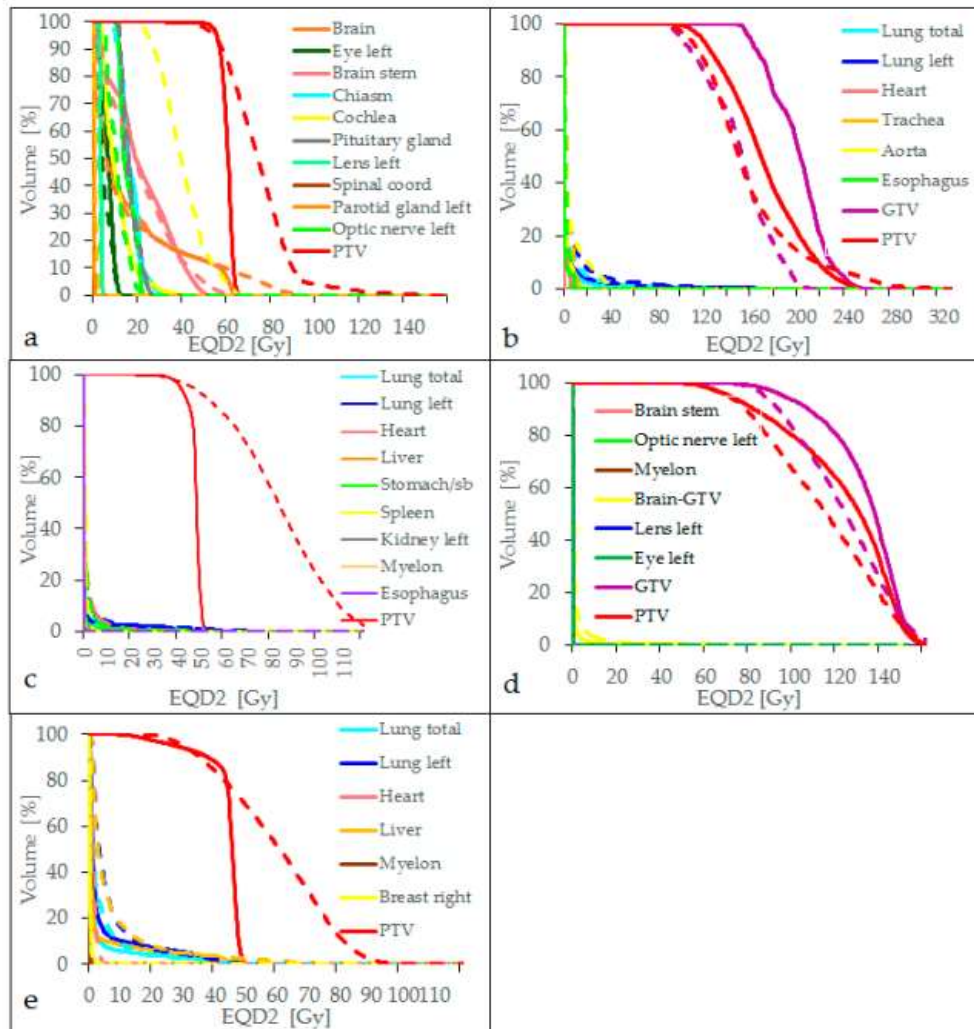


Figure 6: Dose volume histograms for the five clinical scenarios: (a) glioblastoma resection cavity, (b) lung SBRT, (c) sarcoma bone metastasis, (d) sarcoma brain metastasis, (e) breast cancer. Solid lines represent the clinical treatment plans, dashed lines the MRT plans [5].

1.1 Peak to Valley Dose Rate and Percentage Depth Dose

Peak to Valley Dose Rate (PVDR) is a crucial concept to completely describe radiotherapy, constituting the distance between the doses at the peak and at the valley. The formula used to define this parameter is shown below:

$$PVDR = \frac{D_{peak}}{D_{valley}} \quad (1)$$

It is important to notice that the higher the PVDR the better the treatment of the tumour in the irradiated areas. Besides, it is possible to administer high doses to the tumour at the peak and at the same time to keep the normal cells in the valley unaffected (sparing tissue effect). In this way, the normal tissue cells that are located at the valley can regenerate and repopulate, sending positive signals to neighbouring cells. Simultaneously, due to the Bystander effect, the tumoral cells that receive a high dose send negative signals to adjacent cells intensifying the effect of the therapy. The Bystander effect is an effect that concerns the interaction between adjacent cells or in the immediate vicinity for which it is possible that a signal is emitted by the irradiated cells and, in some way, interact with the other cells not directly affected, stimulating a response by these unaffected cells.

Our aim is to implement this technique by increasing the PVDR as much as conceivable to improve the efficiency of the MBRT.

1.2 Radiobiology

The biological mechanisms which underlie the treatment with MBRT are mostly unknown and many hypotheses have been proposed to explain the effectiveness of this technique. Substantially, the radiation targets at the tumour and causes tumour cell DNA double strand breaks, which leads to cell death and consequentially tumour control. Although radiation is effective on tumour control, the risk of unacceptable collateral radiation damage to the surrounding normal tissue, especially the one of nearby sensitive organs, often prevents radiation oncologists from prescribing the high radiation dose needed for tumour control. We have only recently begun to understand the effects of radiation on cells beyond the cytotoxic effect, such as the bystander effect, the abscopal effect, dose-volume effect, and radiation-induced anticancer immune responses.

As aforementioned, several studies have reported the therapeutic interest of MBRT at preclinical level, however, the biological mechanisms responsible for the described protection of healthy tissues are not fully understood to date. Classically, the protective effect of MBRT on healthy tissues has been associated with the apparent resistance of normal tissue vasculature to MBRT [6]. Furthermore, it has been proposed that the efficiency of MBRT on reducing tumour growth is related to a preferential damaging effect on the tumour vasculature (Figure 7) [7].

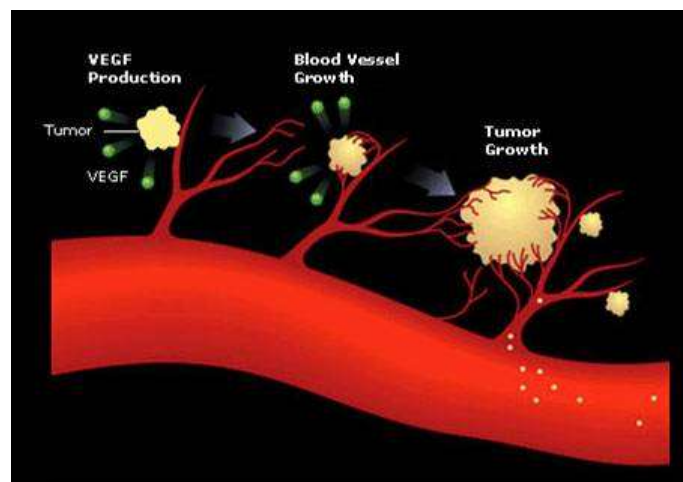


Figure 7: Diagram illustrating the formation of new blood vessels that support tumour growth (angiogenesis) [8].

It is well known how hypoxia represents a fundamental factor for tumour growth, inducing the expression of growth factors that stimulate blood vessel formation into and around the tumour. Subsequently, interactions among the tumour cells, surrounding tissue cells, and immune cells begin to collapse, leading to eventual metastasis to distant sites. It has been hypothesized by these studies that immature blood vessels in a tumour would be more sensitive to MBRT while the healthy tissue mature blood vessels would be resistant to MBRT. Additionally, several reports have shown how MBRT affects the tumour vascular structure, even though, the effect may vary depending on the tumour type. Finally, MBRT induces a decrease in tumour blood vessels leading to a decrease in perfusion and, consequently, to tumour hypoxia [9, 10]. Although MBRT

preferentially affects the tumour vasculature structure, we should always take into consideration the other effects that MBRT may cause.

1.3 Recent developments

The proof of the effectiveness of MBRT in recent years led to the development of other radiotherapy techniques, such as the proton MBRT. This therapy was evaluated by Paucelle et al. in 2015 [11], at Institute Curie - Proton Therapy Center, Orsay, France – with the aim of providing a therapy which uses both MBRT and Proton Therapy. Particularly, the technique combines the advantages of spatially fractionated dose, the tissue sparing effect, and the proton source, the Bragg peak. In fact, by irradiating a radiochromic film at different depths, it is verified that the pattern of the dose in the normal tissue is maintained while at the Bragg peak there is a homogeneous distribution of the dose (Figure 8) [11]. If the Bragg peak corresponds to the position of the tumour it is possible to improve the efficiency of the therapy by giving the maximum dose at the tumour and at the same time preserving the normal tissue before.

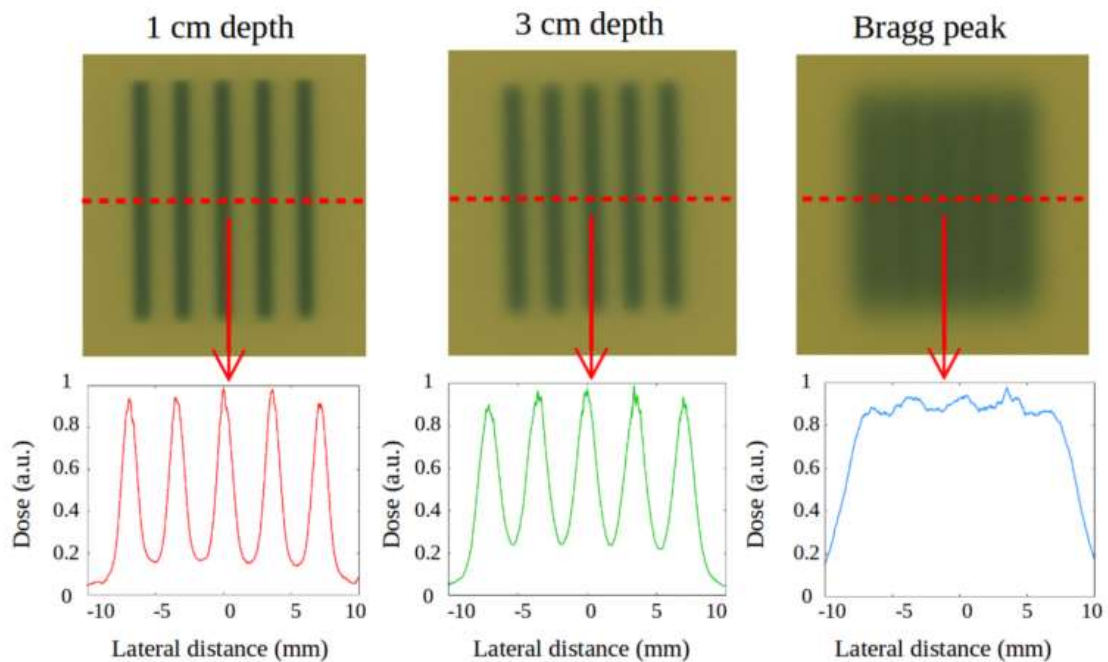


Figure 8: Dose distribution at different depth of film irradiated with pMBRT [11].

Recently, due to the validation of FLASH RT for the treatment of tumours, a research group proposed a new concept of small animal X-ray irradiator based on a conventional imaging X-ray tube for preclinical research which showed its feasibility to deliver FLASH dose rates [12].

FLASH therapy, meaning the delivery of a substantial dose fraction at ultra-high dose rates (UHDR) [13], is typically characterized by dose rates of 2 Gy in a fraction of seconds/minutes in comparison to the conventional therapy in which the standard dose rates are around a few cGy/s. FLASH irradiations significantly reduces normal tissue toxicity compared to conventional radiotherapy, while maintaining tumour control probability at a similar level [14]. However, the underlying biological mechanisms remain unknown.

Once verified the possibility to release the UHDR with a conventional X-Ray tube, commonly used for imaging, they would improve the MBRT technique overlapping the FLASH therapy. The choice of a conventional X-ray source was motivated by the low price, high availability, and wide variety of models.

A study in 2023 designed a small animal X-ray irradiator using a conventional X-ray head for imaging and studied its feasibility in delivering FLASH dose rates. This consists of two sets of dose measurements made by common rotating anode X-ray heads from Toshiba, models E7869X (Toshiba E7869X PI) and E7252X (Toshiba E7252X PI). Both sources can produce beams with either small (0.6 mm) or large (1.2 mm) focal spots, while the maximum tube potential is 150 kVp [12]. The tube filtration is made with aluminium thickness in the order of 0.9 to 1 mm (Figure 9).

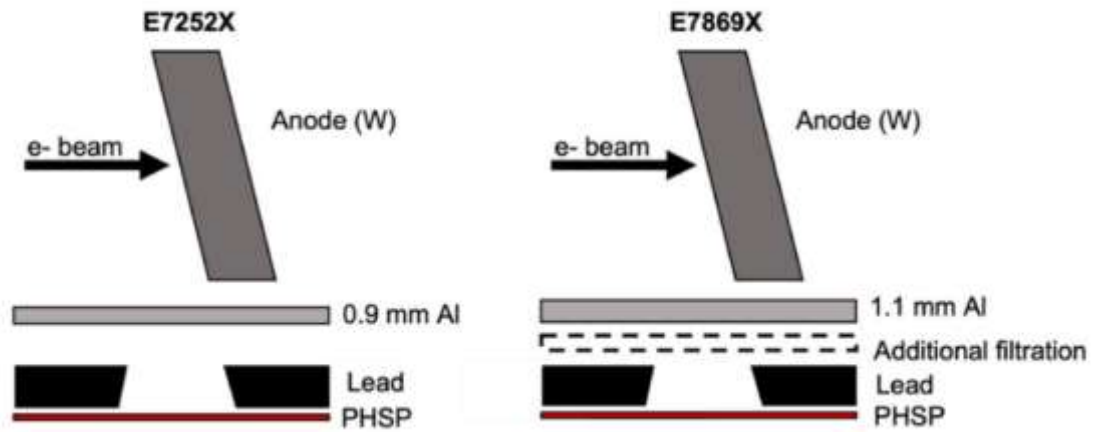


Figure 9: Two configurations of the X-ray tube for the irradiation [12].

The analysis consists of simulations using Monte Carlo simulation (TOPAS) and experimental data using dosimetry to obtain the condition of the maximum irradiated dose. The results show that the E7252X system could deliver the maximum dose, together with the ability and repeatability of administering very short pulses, once compared with other studies [12].

Chapter 2: Monte Carlo simulations

A fundamental part of the thesis involves Monte Carlo simulations to find the most suitable configuration of irradiation using MBRT technique. For this purpose, I used TOPAS (TOol of PArticles Simulation), a toolkit developed from Geant4. The aim was to mark the dose distribution in a phantom (either Plexiglass or Water) and observed the pattern of irradiation of MBRT using an X-Ray source. I examined the output of the simulation to define the PVDR of different MBRT configurations.

2.1 TOol of PArticles Simulation (TOPAS)

In recent years, the interactions between particles and matter became a significant field to investigate in view of the medical application of ionizing radiation. The interactions between the particles are governed by the Monte Carlo method statistics, which represent a complex subject of study. For this reason, it was developed Geant4 free software package, which is composed of tools for the accurate simulation of the transition of particles through matter [15]. All aspects of the simulation process have been included in the toolkit, listing the:

- Geometry of the system.
- Materials involved.
- Fundamental particles of interest.
- Generation of primary events.
- Tracking of particles through materials and electromagnetic fields.
- Physics processes governing particle interactions.
- Response of sensitive detector components.
- Generation of event data.
- Storage of events and paths.
- Visualization of the detector and particle track.
- Analysis of simulation data at different levels.

Geant4 simulations aimed to use C++ programming to set up all the parameters or configurations needed, and the package presents numerous physics models to handle the interactions of particles with matter across a very wide energy range [15]. On the other hand, TOPAS turned out to be a much more intuitive tool than the others and did not require knowledge of C++ programming, even though it is based on Geant4 physical models. TOPAS is a code developed from the Monte Carlo simulation programs (Geant4) at first to improve the proton therapy. Consequently, employed by physicists in research or in medical field for common radiotherapy and medical imaging applications [16]. The basic concepts of TOPAS were originally created in 2009 by an NIH-funded collaboration from the SLAC National Accelerator Laboratory, Massachusetts General Hospital, and the University of California in San Francisco, and they constantly change. It was possible to request a personal license for medical or university research purposes attending a short course. A novel TOPAS version 3.8 was released in 2022, fixing different bugs.

It has been shown in some studies that the use of Monte Carlo simulations reduces the uncertainty of radiotherapy treatment plans, which can manifest different collateral effects [17].

Consequently, the project aims to create a toolkit specialized in simulation that:

1. Preserves the underlying Geant4 code.
2. Provides all the features of Geant4 in terms of speed, accuracy, and flexibility.
3. Offers well-compared basic physics.
4. Supports users who have limited or no programming skills [16].

TOPAS is designed as a "user code" overlaid on Geant4 and it includes the standard Geant4 toolkit, plus additional code to make Geant4 easier to control and extend its functionality. TOPAS allows the user to produce simulations which are both "reliable" and "repeatable" [18]. "Reliable" means both accurate in physics and with a high probability of simulating exactly what the user intended

to simulate, reducing the issues correlated to wrong units, incorrect materials or scoring positions, etc. "Repeatable" means not only getting the same result from one simulation to another but being able to easily restore a previously used configuration and reduce sources of error when a configuration is shared from one user to another. TOPAS is executed by users as a command-line program that includes the name of the top-level parameters file. This file includes all the other necessary parameter files (Figure 10), making TOPAS divisible into blocks thanks to which errors decrease and the same components can be reused for other simulations.

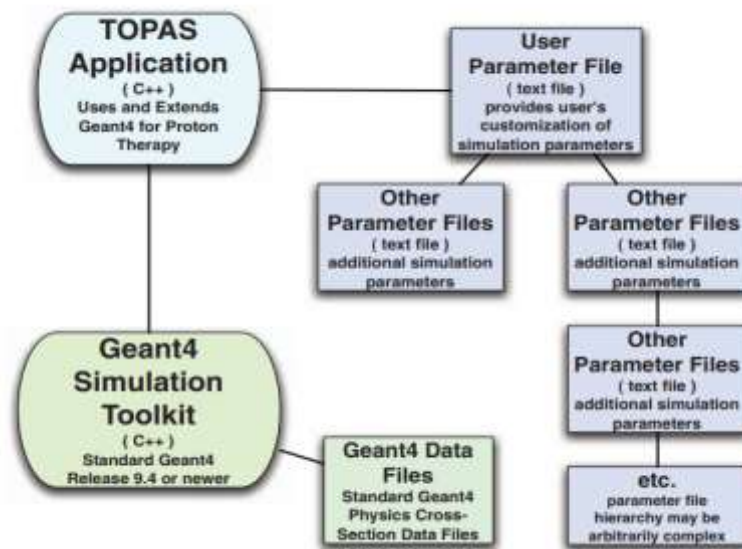


Figure 10: Workflow chart in TOPAS [18].

TOPAS users can configure pre-built components to simulate a wide variety of radiotherapy and examples of some of the main configurations are available to the user. Besides, by changing the examples parameter file it is possible to adapt them to a specific simulation. Each parameter file is a simple text file consisting of one or more lines, which specifies an included file or parameter definition [18]. The order of lines within a parameter file is not significant, eliminating a potential source of user error. Declaring the features of parameter files is possible to specify everything in the simulation, so the main parameter files available are listed below:

- Geometry (“Ge”)
- Particle sources (“So”)
- Physics (“Ph”)
- Score (“Sc”)
- Graphic (“Gr”)
- Temporal characteristics (“Tf”)

Within the parameter files, the "Parameter_Type" must be declared:

- «s» = string
- «b» = Boolean
- «i» = integer
- «d» = double

TOPAS supports “relative parameters,” wherein one parameter may be set relative to another [18]. Also, it is possible to include in a parameter file other parameter files through ‘IncludeFile’ declarations. In this way, the file name is significant, so it must be written carefully. The command line can appear in any position in the parameter file and can use either absolute or relative file positions. A file inherits all settings from its ‘IncludeFile’ statements and can override any of those included conditions by setting the same parameter name to a new value (Figure 11) [18].

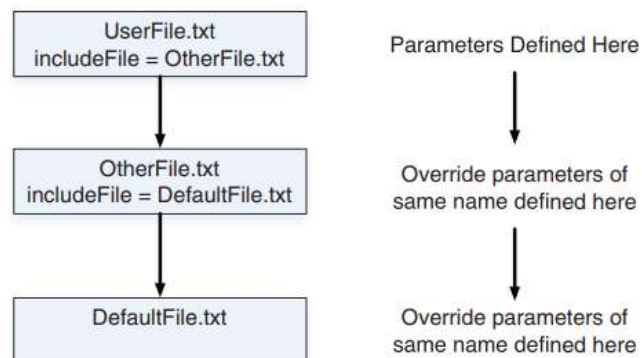


Figure 11: Chart of the include mechanism in TOPAS, the UserFile pulls in additional parameters defined in the OtherFile which in turn pulls in parameters defined in the DefaultFile [18].

TOPAS enables users to work separately on a single part of the entire simulation code, where the overall parameter file contains others sub file which define specific characteristic (i.e. declaration of geometry, patient, source, etc) (Figure 12).

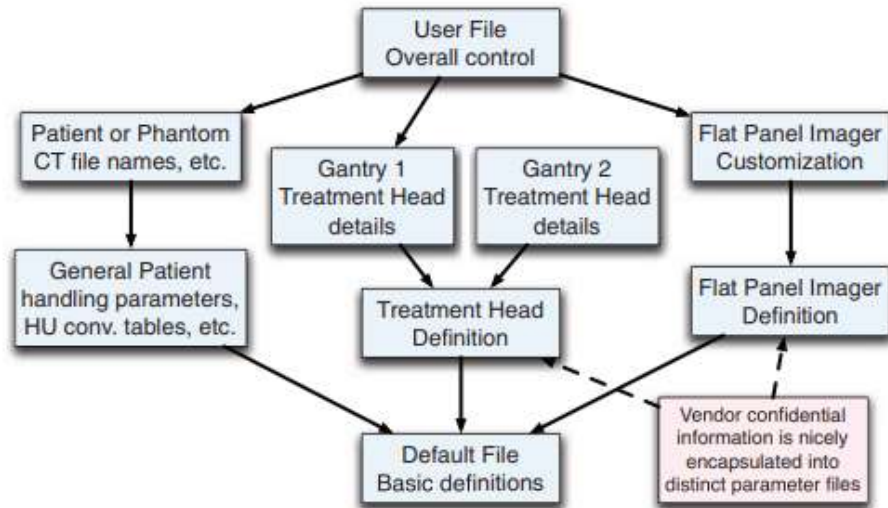


Figure 12: Multiple chains of parameter files. The UserFile extracts in parameters from patient, gantry and imager files. Values from the UserFile override values from the other files [18].

One of the reasons why the software is user friendly is that the structure of the file is represented by a construction in which the constitutive bricks can be easily and intuitively modified. Besides, the code castoff by users in TOPAS is more straightforward than the Geant4 one, as shown in Figure 13.

<pre> #include "BIDetectorConstruction.hh" ... #include "G4RunManager.hh" #include "G4HistManager.hh" #include "G4Box.hh" #include "G4Tubs.hh" #include "G4LogicalVolume.hh" #include "G4PVPlacement.hh" #include "G4SystemOfUnits.hh" ... G4VPhysicalVolume* BIDetectorConstruction::Construct() { G4RunManager* nist = G4RunManager::GetInstance(); G4bool checkOverlaps = true; G4double world_sizeXYZ = 1.; G4Material* world_mat = nist->FindOrBuildMaterial("G4_AIR"); G4Box* solidWorld = new G4Box("World", 0.5, 0.5, 0.5); G4LogicalVolume* logicWorld = new G4LogicalVolume(solidWorld, world_mat, "World"); G4VPhysicalVolume* physWorld = new G4PVPlacement(0, G4ThreeVector(), logicWorld, "World", 0, false, 0, checkOverlaps); G4Material* cylinder_mat = nist->FindOrBuildMaterial("G4_WATER"); G4Tubs* solidCylinder = new G4Tubs("Cylinder", 0.4, 0.2, 0, 0deg, 360*deg); G4LogicalVolume* logicCylinder = new G4LogicalVolume(solidCylinder, cylinder_mat, "Cylinder"); new G4PVPlacement(0, G4ThreeVector(), logicCylinder, "Cylinder", logicWorld, false, 0, checkOverlaps); ... return physWorld; } </pre>	➔	<p>Equivalent TOPAS Parameters</p> <pre> s:Ge/World/Material = "G4_AIR" s:Ge/Phantom/Type = "TsCylinder" s:Ge/Phantom/Parent = "World" s:Ge/Phantom/Material = "G4_WATER" d:Ge/Phantom/RMax = 40. cm d:Ge/Phantom/HL = 20. cm </pre>
--	---	--

Figure 13: Examples of two programs written in Geant4 code (left) and TOPAS code (right) [18].

TOPAS offers two significant instruments, namely the User Guide and User Forum, which are indispensable for users to custom simulation on TOPAS. The first one provides a detailed description of the possible parameter files, while the second one gives the opportunity to ask questions to other users regarding the use of TOPAS or its structures. The software has been successfully applied to research in radiation therapy physics and macroscopic organ/cellular biology. Nevertheless, more fundamental research is needed to understand the underlying mechanisms of radiation, oxygenation, intracellular signalling, drug-induced radiation sensitization or resistance, etc. [19].

TOPAS-nBio, a library of extensions for the main TOPAS system, has been recently developed [19]. On these terms, the main parameter files remain unchanged while a new parameter has been added to specify the chemistry (Ch) and scoring to specifically describe the kinetics of DNA-radiation interaction. TOPAS n-Bio is based on Geant4-DNA and it provides nano or submillimetre geometry and precises parameters such as nucleus or proteins.

At last, TOPAS represents a powerful simulation tool, more straightforward than Geant4 while preserving its main features, such as repeatability, reliability, and a great flexibility in the definition of the parameters. Thanks to the block architecture, it promotes collaboration around the world to share the knowledge.

2.2 Simulation set-up

In our MC simulation, the output was a 2D dose distribution in a modelled gafchromic film (PET) placed in a phantom (Plexiglass or Water). I scored the dose released by the interaction between primary particles (photons) of X-Ray source and the materials. The main features of the source were set in order to simulate the HSR system (X-Rad 225 XL) used for the experimental tests: maximum energy about 225 kV and 0.3 mm Cu added filtration. The TOPAS simulation file was based on a previous code developed by C. K. Akbas, now

customized for our requirements. The number of primary photons simulated was 3.2×10^{10} . The simulated X-ray source ($3.5 \times 3.5 \text{ mm}^2$ focal spot) with flat distribution generated a cone beam which was rectangularly shaped by two lead apertures at the bottom of steel cylinders placed after the source (first aperture: 15.3 mm, second aperture: 14.4 mm), while the collimator was located at the end of the system (Figure 15).

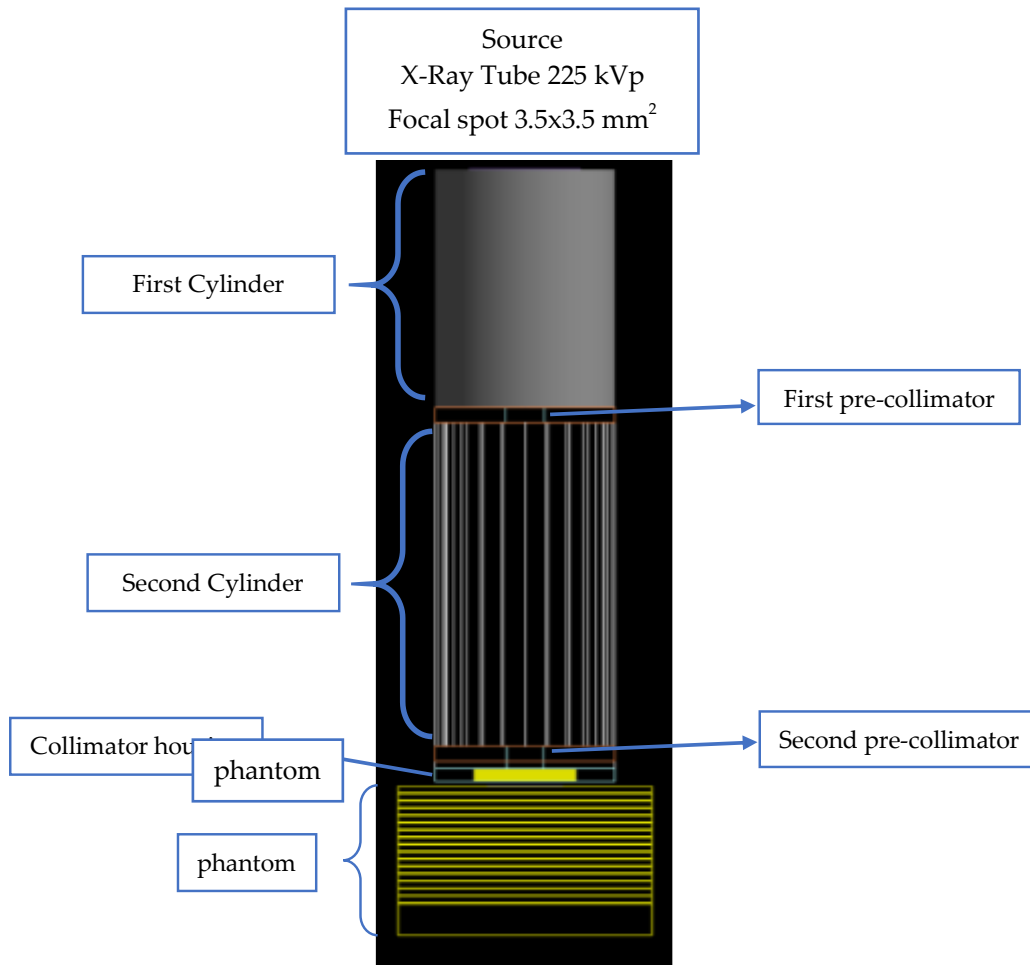


Figure 15: Scheme of geometry from TOPAS GUI constitute from the top by an extended source, two cylinders to collimate the beam (bottom aperture about 15.3 mm and 14.4 mm) in grey, the housing of the collimator (yellow) and the phantom in PMMA (yellow).

Collimators were used to spatially fraction the broad beam into mini beamlets by changing the following features: parallel and divergent slits, different materials, and the pattern. The irradiation was made in planar mode and the configuration is shown in Figure 15. Consequently, I changed the configuration to generate a rotational irradiation of the phantom, obtaining four different views.

2.2.1 Collimator

The basic collimator needed to simulate MBRT technique is composed of parallel beamlets 1 mm spaced with an aperture ranging from 200 to 500 μm . In this project, I implemented different collimator geometries through TOPAS with a variable aperture, using various materials to shape the X-Ray beam into mini beamlets. I changed the parameter file 'TsBox' to simulate the collimator components and I positioned them in the collimator housing simulated by 'TsBox'. The first collimator used was made by lead (Pb) 5 mm thick, beamlets 40 mm length and 0.5 mm width with 1 mm centre-centre distance, spacing with PET¹ beamlets (Figure 16).

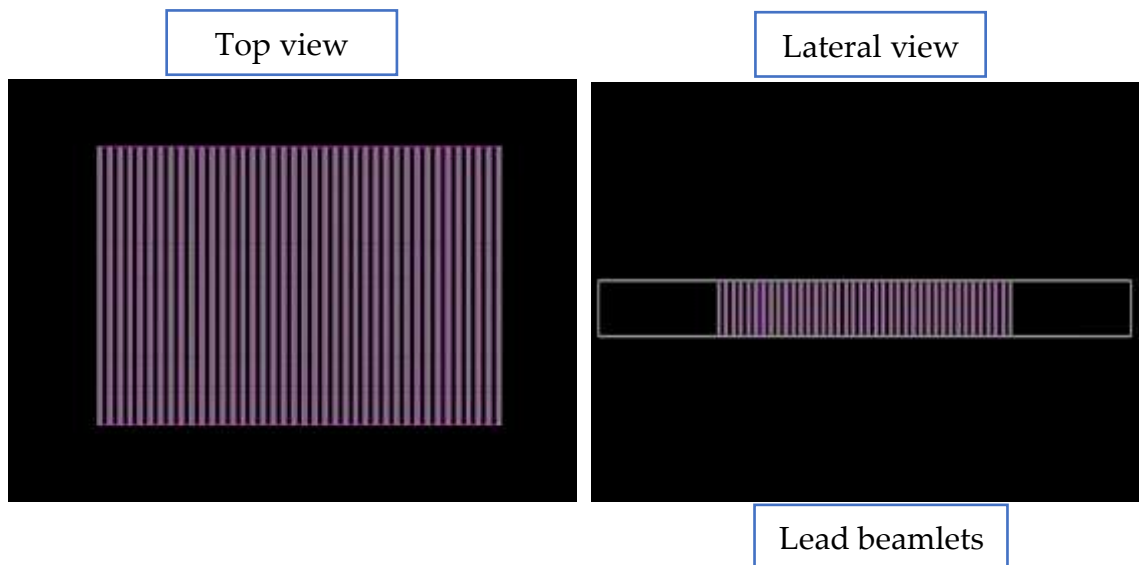


Figure 16: Image from TOPAS GUI of the simulated lead slits (grey) and PET slits (violet) top view (left) and lateral view (right).

Therefore, while maintaining the same material and features, I changed the pattern to obtain collimators with beamlets of 0.2, 0.3, 0.4 mm width 1 mm spacing. I utilized various materials during this phase to establish a configuration that was much more straightforward to operate on real, as the lead is a costly and unsaturated material has very low malleability. I decided to simulate the same

¹ PET: Polyethylene terephthalate (or poly(ethylene terephthalate), PET, PETE, or the obsolete PETP or PET-P), is the most common thermoplastic polymer resin of the polyester family.

pattern previously described but using brass as material (Figure 17). For this purpose, it was necessary to increase the collimator thickness since brass is notoriously less shielding than lead. More particularly, the thicknesses selected for the brass collimator were 10, 20, 30 mm to reduce the background caused by the no shielded beam.

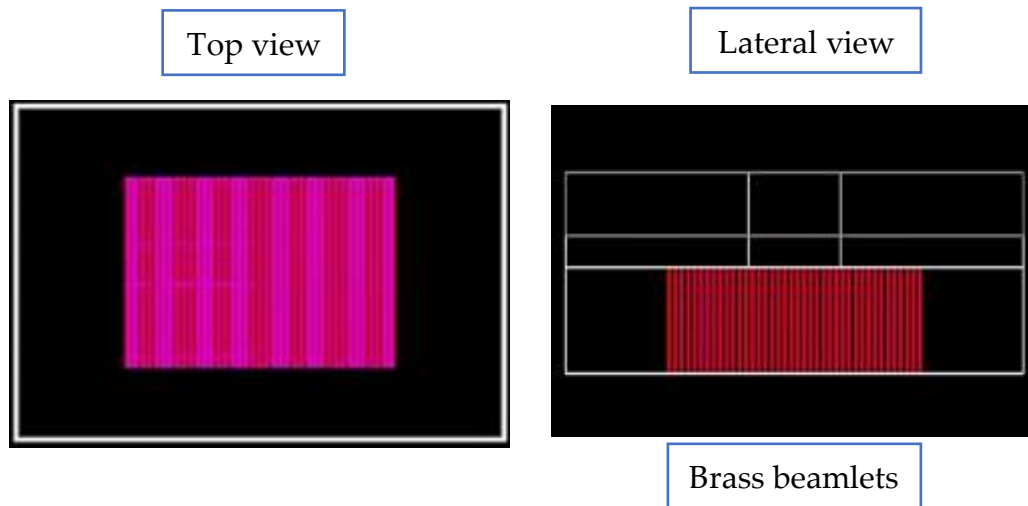


Figure 17: Image from TOPAS GUI of the simulated brass slit (red) and PET slits (violet) top view (left) and lateral view (right).

Because of the high thickness of the collimator, the cone beam used did not pass through the lateral slits, due to the minimum acceptance angle. To improve the irradiation, I set a new brass collimator of 40 mm thick with divergent slits of 0.5 and 0.3 width (Figure 18). To determine the tilt angle of beamlets I used the distance source-object (collimator centre) and the distance centre-slits of the collimator to obtain the tangent of the angle.

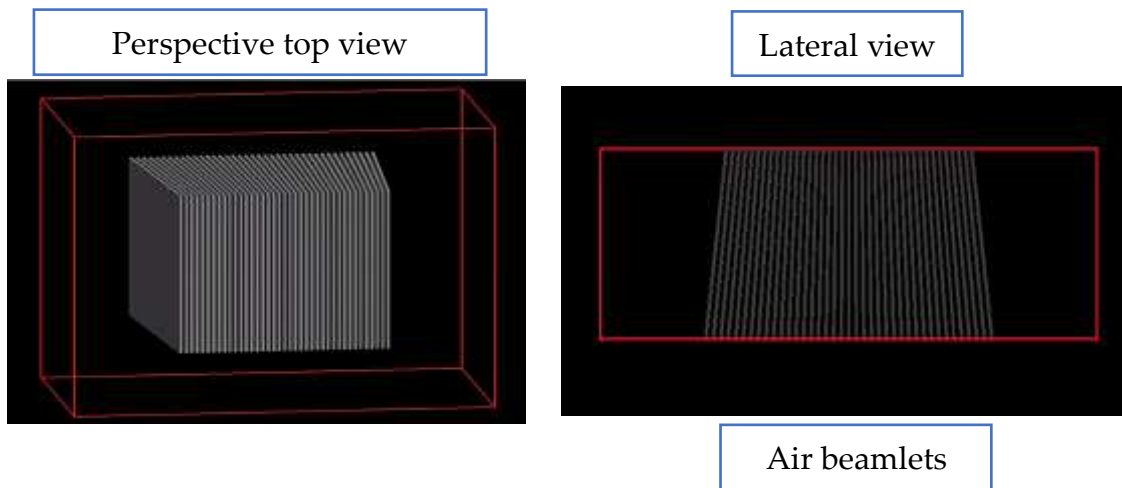


Figure 18: Image from TOPAS GUI of the simulated air slits (grey) in a brass box (red) perspective top view (left) and lateral view (right).

2.2.2 Energy scoring

I simulated the scoring of the dose released at a film made of PET, and through the 'DoseToMedium' command in the simulation I created a .bin file output, consequently, was read via Matlab. The size of the film was defined in the .txt file by changing the geometry parameter and the rebinning determined the width of each pixel. In this specific case, the film varied between 2x2 and 4x4 cm², and along the X and Y axis I set 400 bin. Films were placed in a phantom, previously made of PMMA and then of water, at determined positions.

2.2.3 Phantom

Phantom geometry was implemented using the parameter 'TsBox' in TOPAS, declaring all features. Specifically, I set the material (water or plexiglass), dimensions (x, y, z), and position in the model. Two main phantom geometries were analysed for the simulation:

- Water box in a plexiglass box to simulate the real phantom of the laboratory in which 5 films were placed (Figure 19).
- Plexiglass or water boxes interspaced with films (Figure 20).
- Water box in which were placed 25 films with 2 mm spacing (Figure 21).

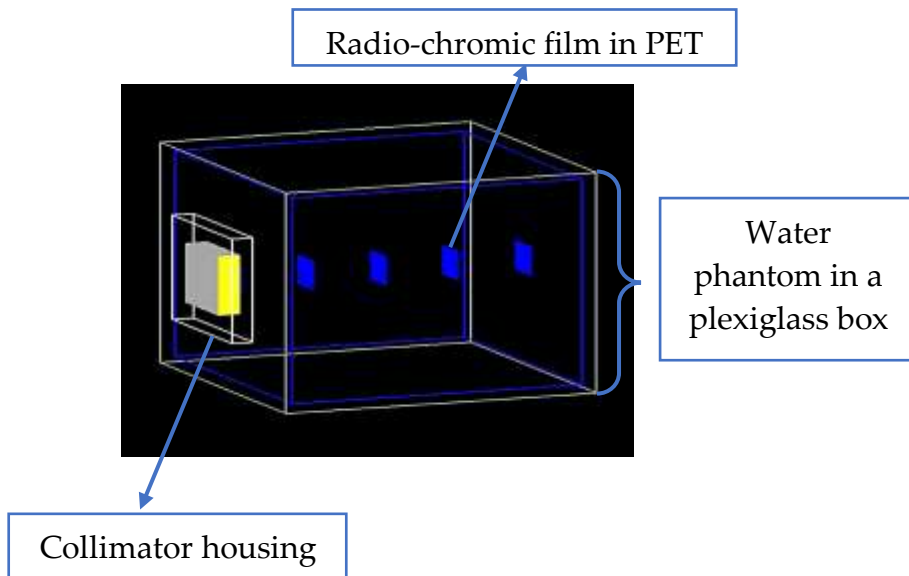


Figure 19: *Traversal view of water phantom ($14 \times 14 \times 14 \text{ cm}^3$) in blue placed in a plexiglass box ($15 \times 15 \times 15 \text{ cm}^3$) in grey, collimator housing in white.*

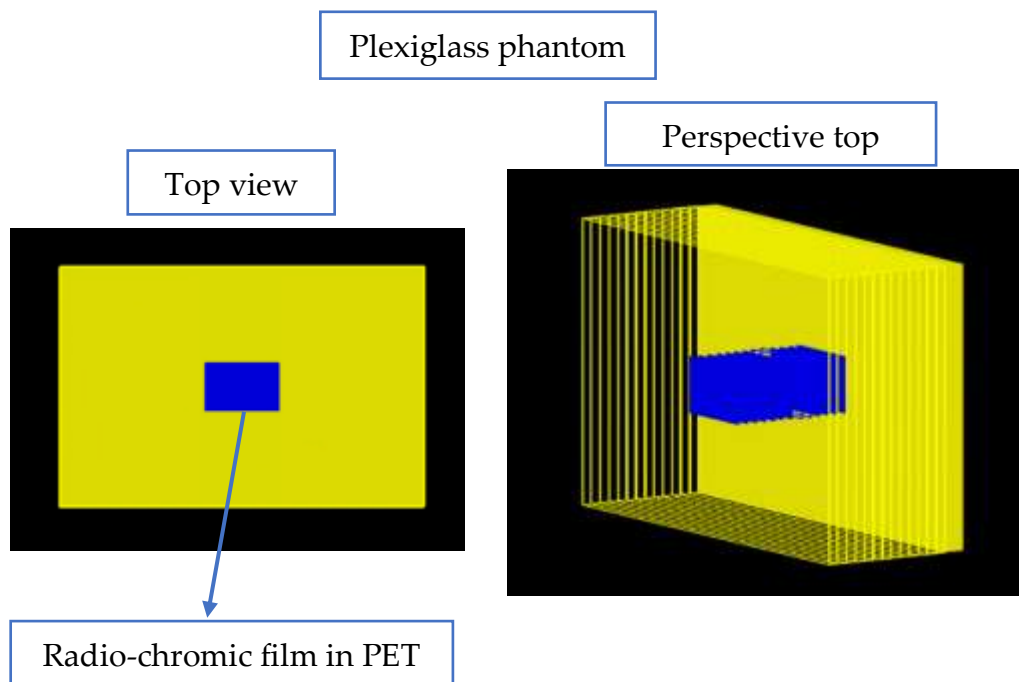


Figure 20: *Top view (left) and perspective top view (right) of a plexiglass phantom ($10 \times 10 \times 5 \text{ cm}^3$) in yellow made of boxes interspaced by films with dimensions of $2 \times 2 \text{ cm}^2$.*

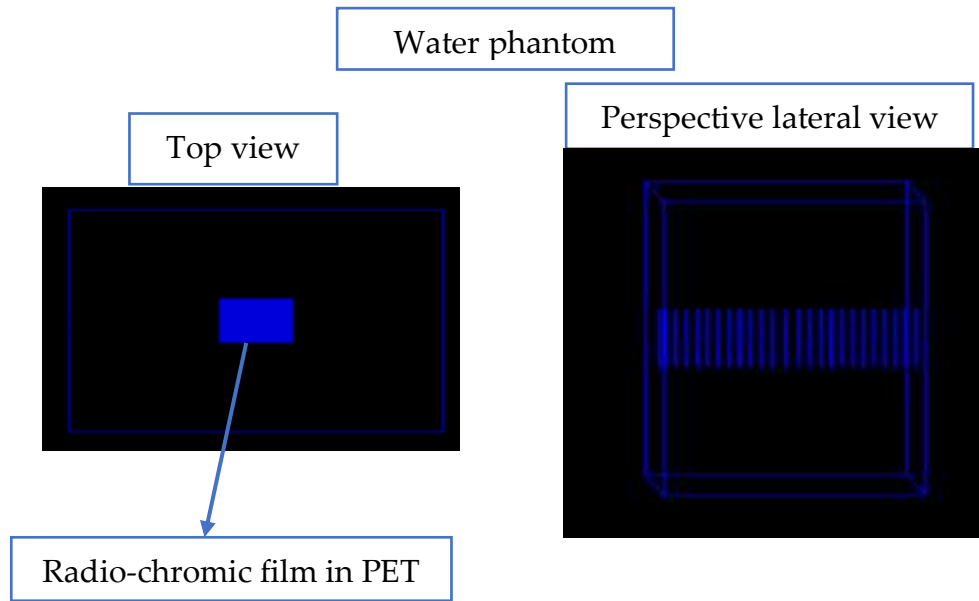


Figure 21: *Top view (left) and perspective lateral view (right) of a water phantom (10x10x5 cm³) in blue, in which I placed 25 films (in blue) with dimensions of 2x2 cm².*

2.3 Simulation results

The results of the TOPAS simulations presented below were obtained through the analysis of the output films. The simulated source was an X-Ray beam at 225 kVp tube voltage; in each simulation the total number of primary photons was 3.2×10^{10} . The output simulation files presented a '.bin' and '.binheader' files for each film, these were converted via Matlab to '.txt' images. The images were displayed and evaluated in ImageJ. I proceeded by selecting a ROI on the first and tenth films and by analysing the dose profile. I examined the dose map changing in depth, highlighted the hypothetical depth beam spread, and determined the PVDR at the central peak. This analysis was made for each different geometric configuration.

2.3.1 MBRT lead collimator

The preliminary MBRT simulation results are presented below and each one represents a different pattern of the MBRT technique, simulated with a lead collimator 5 mm thick in which beamlets were 1 mm spaced and had various width.

In particular, the phantom used is the one shown in Figure 18, made of PMMA. I often changed the material phantom to Water in the simulation file, leaving the geometry phantom unaffected.

The simulation presented in the following was done with lead MBRT collimator and beamlets with a width of 0.5 mm. The output shows the beam spread in depth caused by the consecutive interaction between the beam and the phantom (i.e. scattering), and the beam cone geometry. The Peak-Valley pattern is highlighted in the dose profile Figure 22 below.

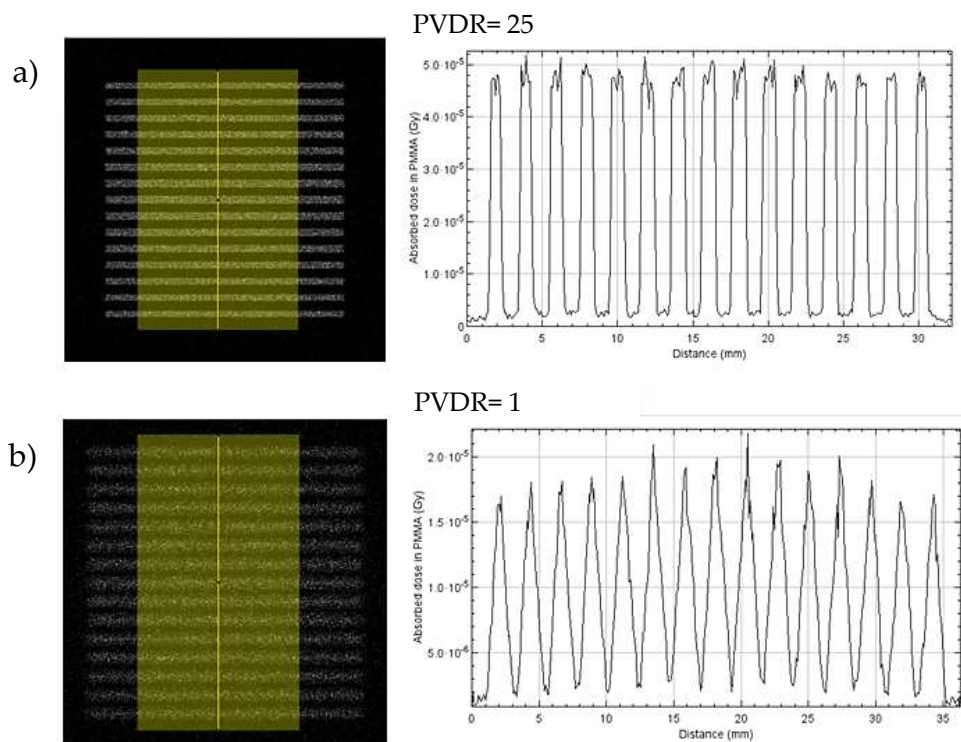


Figure 22: MBRT dose maps (left) and corresponding line dose profiles (right) simulated with a 225 kV, 0.3 mm Cu added filtration, X-ray beam with a multislit collimator (0.5 mm width aperture, 1 mm centre-to-centre distance, 5 mm thick) at a) 0.125 mm and b) 33 mm depth in PMMA.

In the following, I simulated with the same configuration above the MBRT irradiation changing the beamlets width to 0.4, 0.3 and 0.2 mm and analysed alike (Figure 23,24,25).

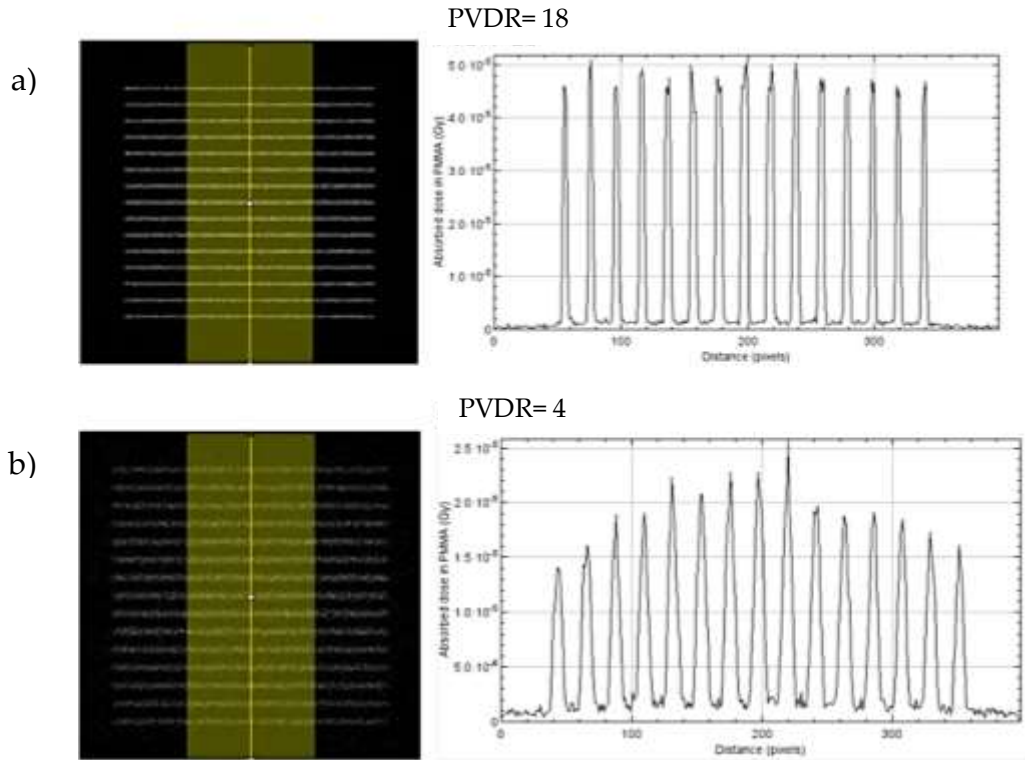


Figure 23: MBRT dose maps (left) and corresponding line dose profiles (right) simulated with a 225 kV, 0.3 mm Cu added filtration, X-ray beam with a multislit collimator (0.3 mm width aperture, 1 mm centre-to-centre distance, 5 mm thick) at a) 2.298 mm and b) 23.88 mm depth in PMMA.

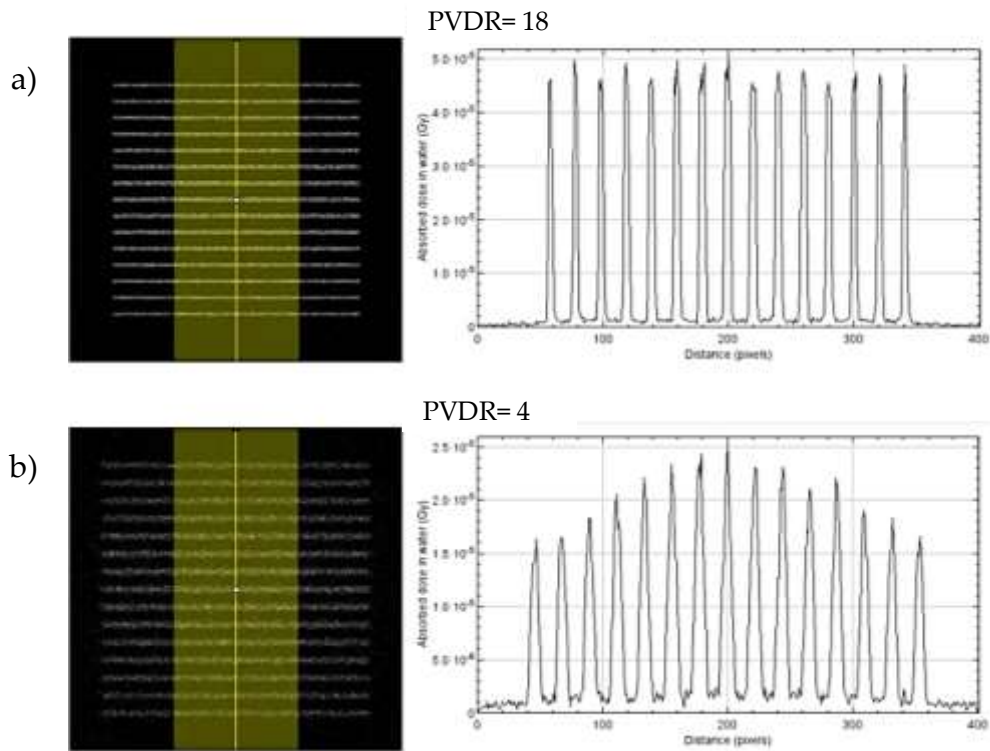


Figure 24: MBRT dose maps (left) and corresponding line dose profiles (right) simulated with a 225 kV, 0.3 mm Cu added filtration, X-ray beam with a multislit collimator (0.3 mm width aperture, 1 mm centre-to-centre distance, 5 mm thick) at a) 2.298 mm and b) 23.88 mm depth in Water.

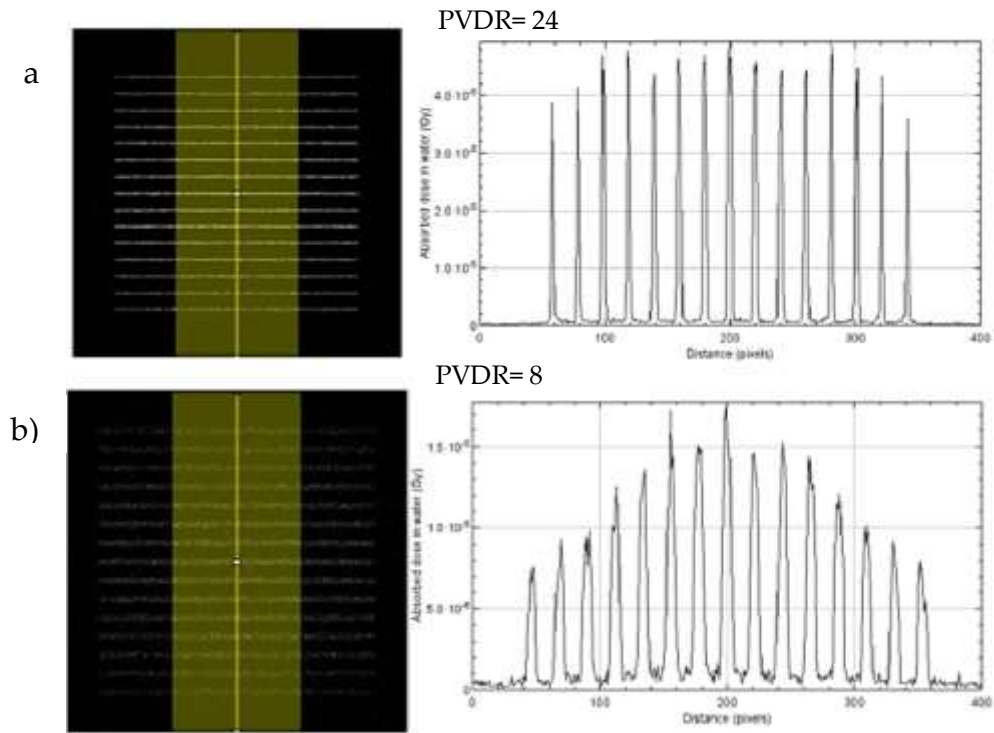


Figure 25: MBRT dose maps (left) and corresponding line dose profiles (right) simulated with a 225 kV, 0.3 mm Cu added filtration, X-ray beam with a multislit collimator (0.2 mm width aperture, 1 mm centre-to-centre distance, 5 mm thick) at a) 2.298 mm and b) 23.88 mm depth in Water.

2.3.2 MBRT brass collimator

To test different materials I choose at first brass, because of its easy availability, low cost and high malleability. Firstly, I simulated MBRT irradiation using a brass collimator 10 mm thick and a X-Ray source generating a beam with angular amplitude of 20 deg. The collimator was placed at the bottom of two cylinders and stuck to the phantom, simulated using a series of boxes in plexiglass interspersed by films (Figure 26).

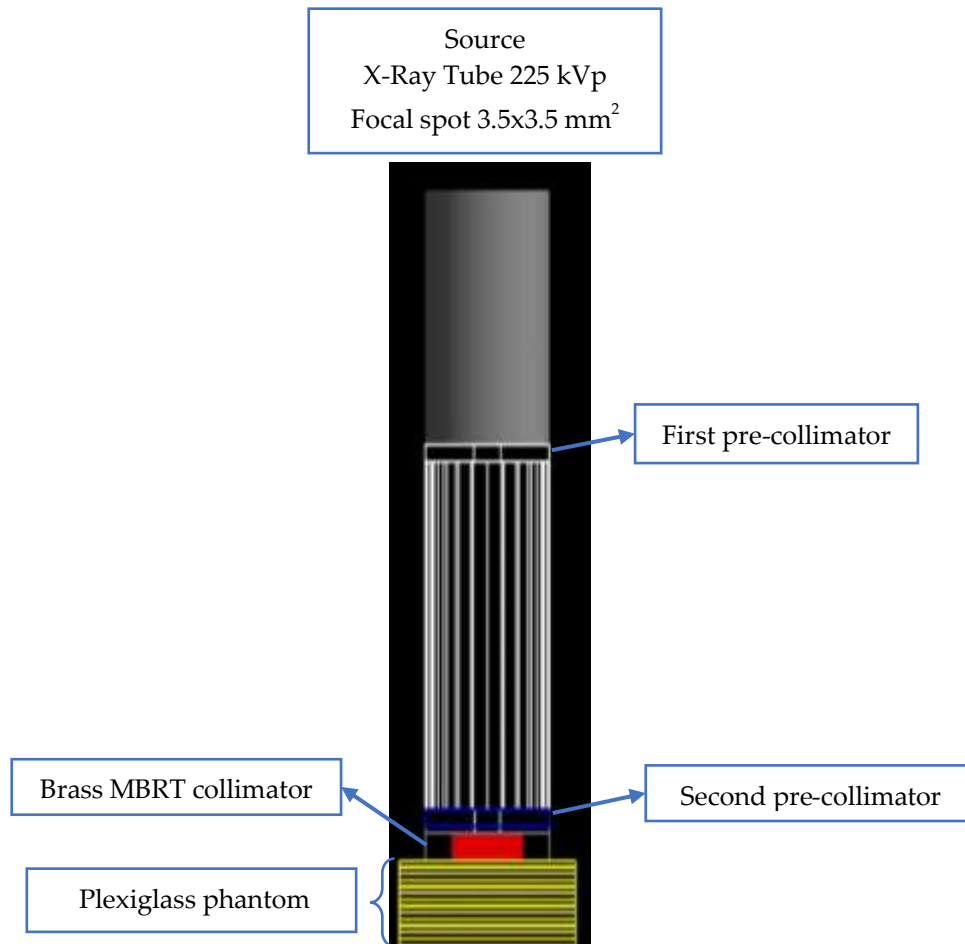


Figure 26: Image from TOPAS of simulated MBRT geometry in brass; lead collimator to shape beam (blue), brass collimator (red) 10 mm thick, PMMA phantom (yellow) 10x10x5 cm³ interspaced with radio-chromic films.

The simulation output was a file in '.bin' and '.binheader' formats, representing the film dose map (Figure 27), showing the dose pattern absorbed in the film (PET). Specifically, I analysed the first and tenth film, corresponding to 2.298 mm and 23.88 mm in depth, respectively, from the bottom surface of the collimator. The output, converted in '.txt' format using Matlab, was opened in ImageJ as an image. The film area was 2x2 cm² in which x and y axis were divided into 400 bin, therefore one pixel corresponded to 0.05 mm. Then, I selected a ROI and made the dose profile (Figure 27). The obtained plot data was transferred in Origin to be analysed using the tool 'multipeak fit', and I calculated the PVDR only for the central peak and the fluctuation was estimated considering the variation of the peaks immediately on the right and left.

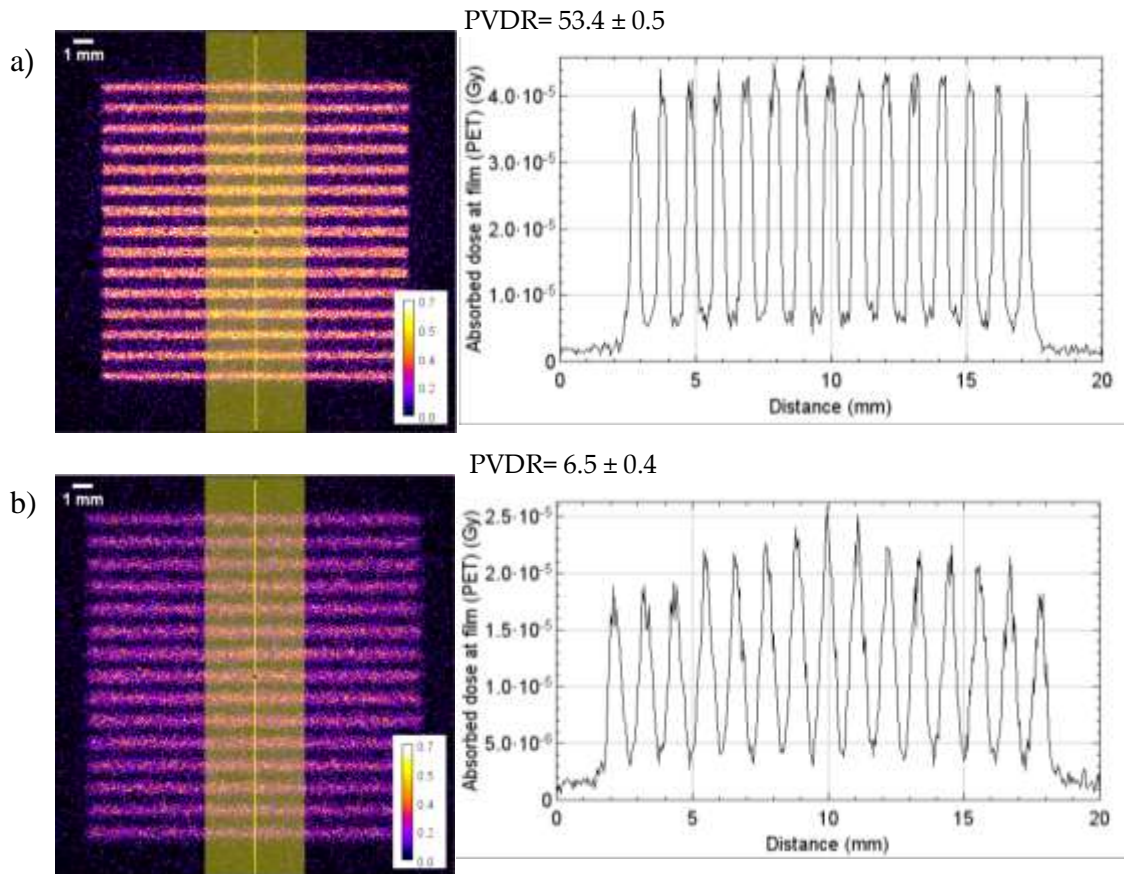


Figure 27: MBRT dose maps in PET (left) (20 mm x 20 mm) and corresponding line dose profiles (right) simulated with a 225 kV, 0.3 mm Cu added filtration, X-ray beam with a multislit brass collimator (0.5 mm width aperture, 1 mm centre-to-centre distance, 10 mm thick) at a) 2.298 mm and b) 23.88 mm depth in PMMA. Number of primary photons is 3.2×10^{10} . Dose values are in units of 10^{-4} Gy.

The dose profile showed evidence of the MBRT pattern of Peak and Valley, however, it was also noted the high background caused by the lower statistic. In depth, it was possible to observe a beamlet widening due to the cone beam shape and the progressive interaction between the beam and the phantom, i.e. scattering.

To reduce the scattering components the collimator thickness was increased. Thus, I simulated the MBRT with a brass collimator of 2 cm thick, an X-Ray source constituted of photons, and a beam angular amplitude of 4 deg. The phantom geometry was the same of the previously presented simulation of 1 cm thick. This simulation results (Figure 28) showed at first the decrease of the background noise in the valley due to the enhancement of the statistic, i.e. increase of interaction events. Consequently, the second effect to analyse was the

penumbra effect caused by the chosen angular which was cut off to be too small to radiate the collimator in its interity. The PVDR at the centre results to be 10 at 2.298 mm (film 1) and about 5 at 23.88 mm (film 10), decreased in depth as was expected. It can be observed how the background noise is better than the one obtained with the collimator with 1 cm thickness, principally due to the smaller angle used and consequentially the increase in the statistic events.

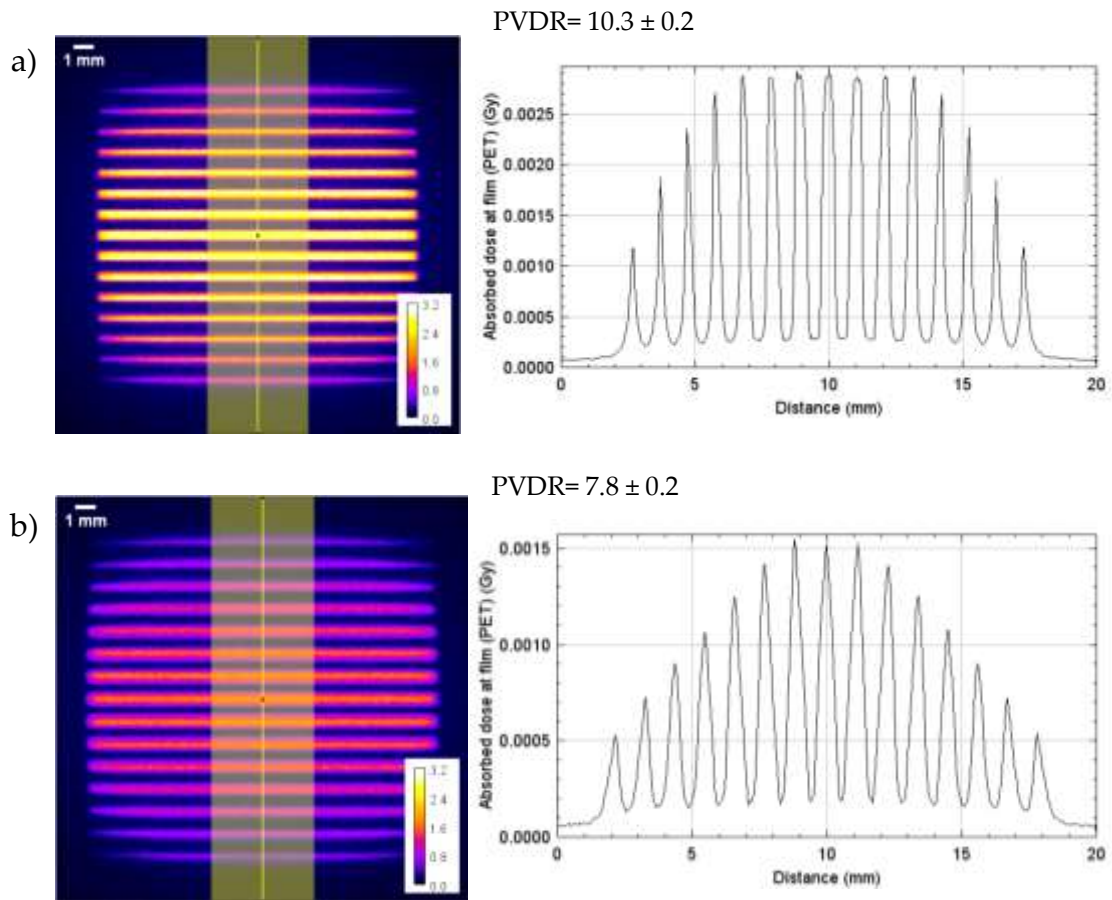


Figure 28: MBRT dose maps in PET (left) (20 mm x 20 mm) and corresponding line dose profiles (right) simulated with a 225 kV, 0.3 mm Cu added filtration, X-ray beam with a multislit brass collimator (0.5 mm width aperture, 1 mm centre-to-centre distance, 20 mm thick) at a) 2.298 mm and b) 23.88 mm depth in PMMA. Number of primary photons is 3.2×10^{10} . Dose values are in units of 10^{-3} Gy.

To further decrease the background dose, I simulated the MBRT with a brass collimator 30 mm thick, an X-Ray beam with a maximum energy of 225 kV, 0.3 mm Cu added filtration, and the beam angular amplitude of 10 deg. It was possible to detect that the typical pattern of the Peak-Valley was maintained in the output film. Furthermore, the output (Figure 29) showed an evident decrease

of the Peak at the side caused by the acceptance angle of the collimator slit. Due to the conic shape of the beam part, this could not pass through the slits and irradiate the film. The background signal still resulted to be higher than what was expected because the beam was not totally shielded.

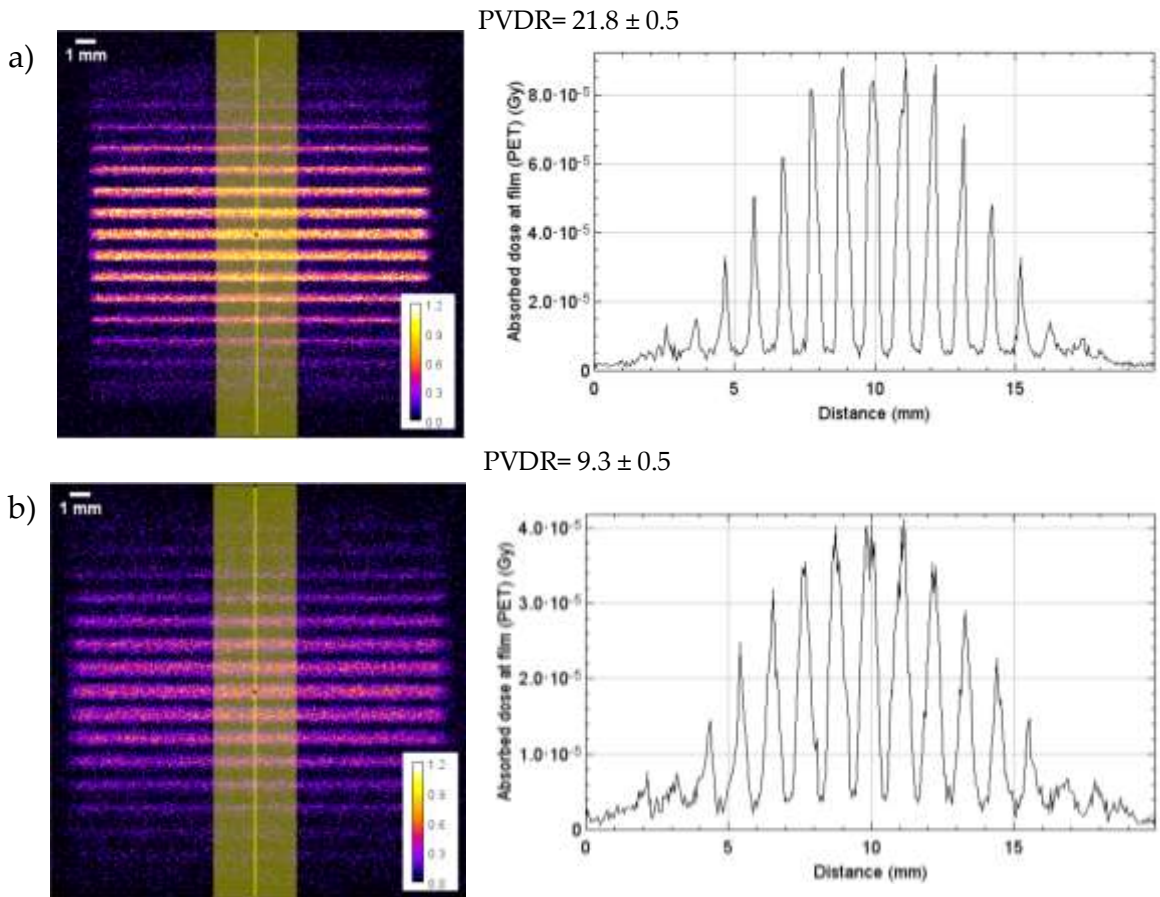


Figure 29: MBRT dose maps in PET (left) (20 mm x 20 mm) and corresponding line dose profiles (right) simulated with a 225 kV, 0.3 mm Cu added filtration, X-ray beam with a multislit brass collimator (0.5 mm width aperture, 1 mm centre-to-centre distance, 20 mm thick) at a) 2.298 mm and b) 23.88 mm depth in PMMA. Number of primary photons is 3.2×10^{10} . Dose values are in units of 10^{-4} Gy.

Consequently, I modified the collimator thickness to 40 mm in order to reduce the background signal and focus the beamlets to decrease the gaussian effect at the peak. This MBRT simulation was realised with a brass collimator 40 mm thick and an X-Ray source generated beam with a angular amplitude of 10 deg. The collimator was placed at the bottom of two cilindrs (Figure 30), while the phantom was simulated using a water box in which were placed films at a

distance of 2 mm (Figure 21). Here, I used two different collimator patterns, one with beamlets of 0.5 mm width and another of 0.3 mm width.

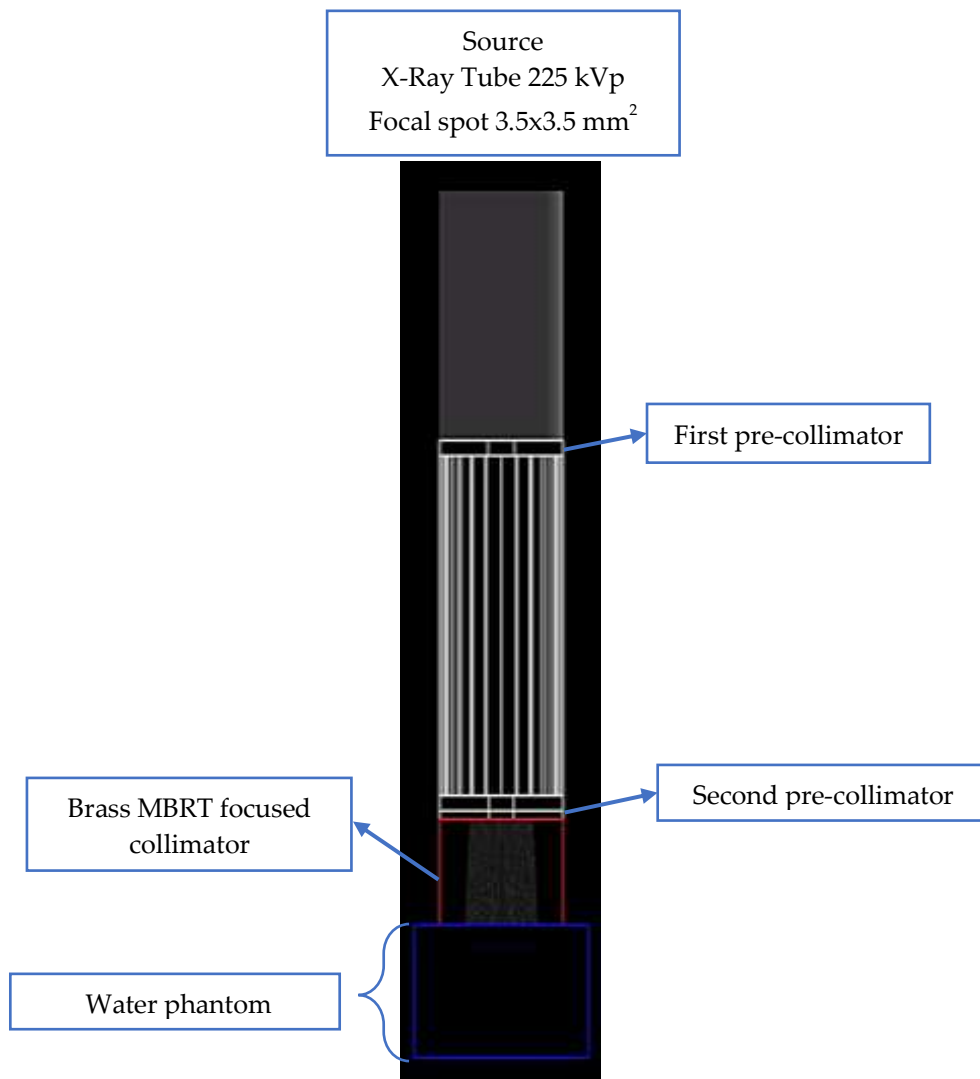


Figure 30: Image from TOPAS of simulated MBRT geometry in brass; lead collimator to shape beam (white), brass collimator (red) 40 mm thick, water phantom (blue) $10 \times 10 \times 5 \text{ cm}^3$ in which are placed 25 films.

At first, it was used the same configuration but with parallel slits to simulate MBRT irradiation with a brass collimator 40 mm thick to enhance the differences with the focused brass collimator that will be next presented. The results (Figure 31) show that most of the lateral beam is lost due to the high thickness of the collimator.

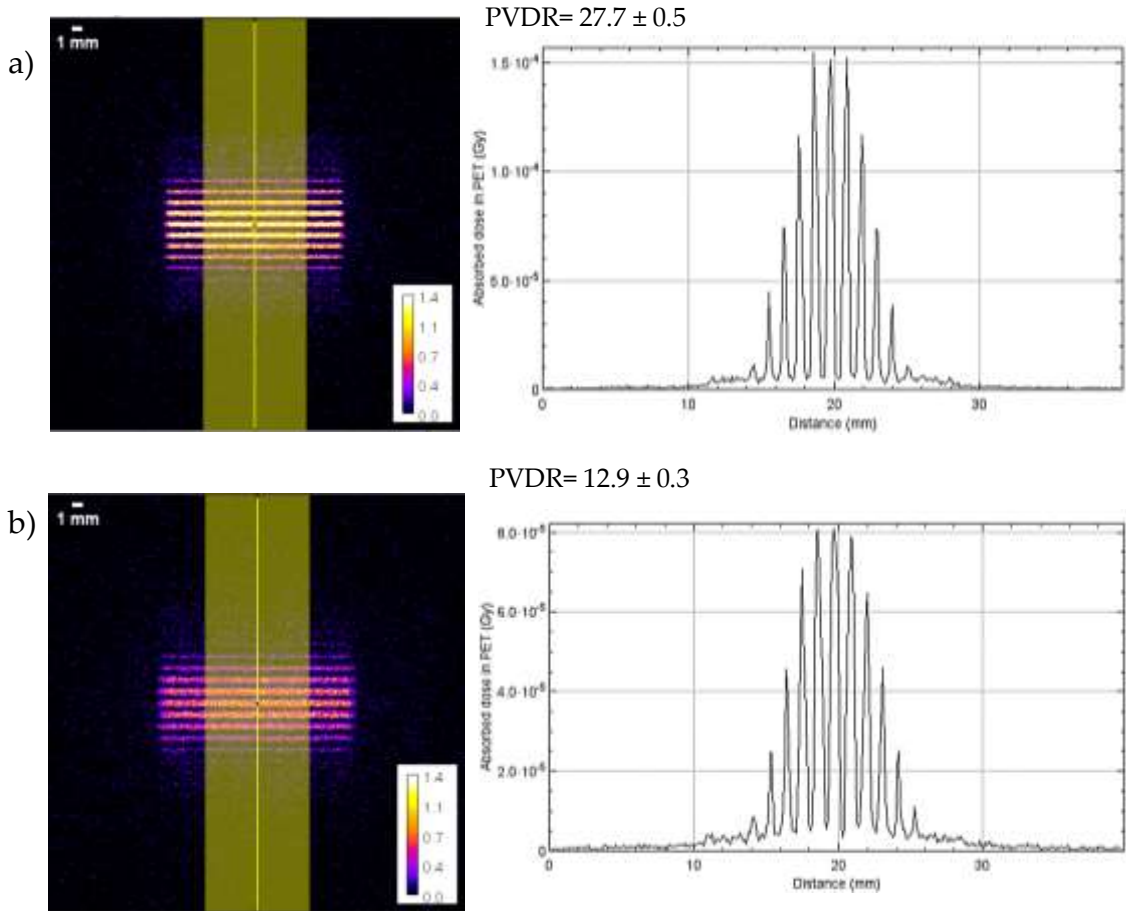


Figure 31: MBRT dose maps in PET (left) (40 mm x 40 mm) and corresponding line dose profiles (right) simulated with a 225 kV, 0.3 mm Cu added filtration, X-ray beam with a multislit brass collimator (0.5 mm width aperture, 1 mm centre-to-centre distance, 40 mm thick) at a) 1.0125 mm and b) 22.3375 mm depth in water. Number of primary photons is 3.2×10^{10} . Dose values are in units of 10^{-4} Gy.

The MBRT focused collimator results (Figure 32 and 33) show the Peak-Valley pattern in dose profile, in which I highlighted the presence of two lateral beams whose peak is smaller than the others. This phenomenon is caused by the fact that the irradiation area of the collimator is smaller than the collimator itself, so that the outermost beamlets are not completely irradiated. The results revealed the effectiveness of beam divergence, since this parameter reduced the lateral peak decreasing effect which could be previously seen with parallel beamlets simulation (Figure 31).

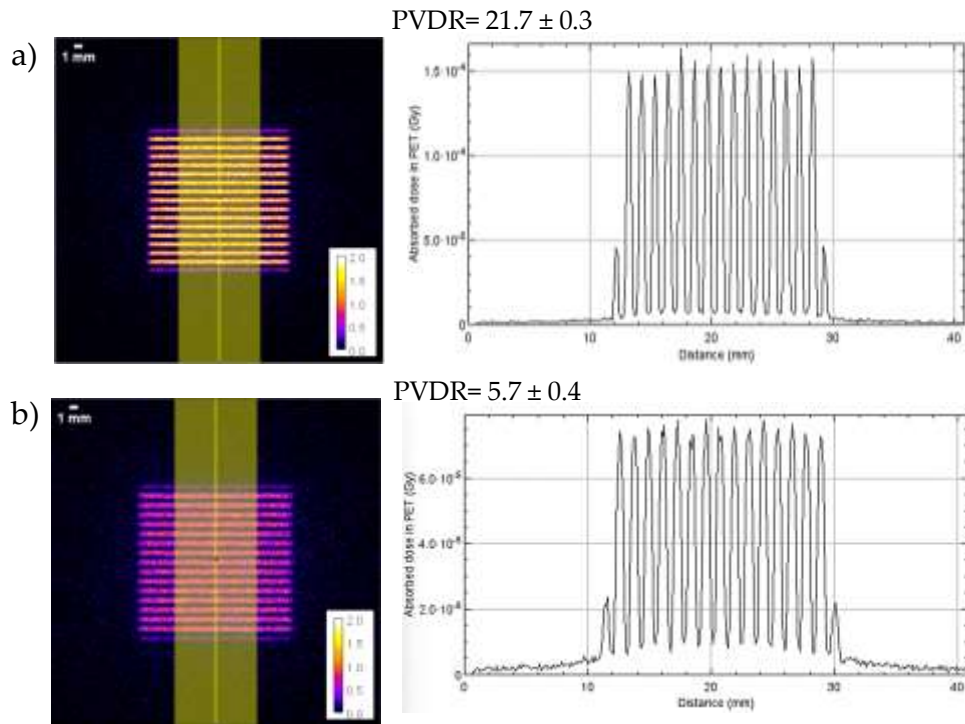


Figure 32: MBRT dose maps in PET (left) (40 mm x 40 mm) and corresponding line dose profiles (right) simulated with a 225 kVp, 0.3 mm Cu added filtration, X-ray beam with a focused multislit brass collimator (0.5 mm width aperture, 1 mm centre-to-centre distance, 40 mm thick) at a) 1.0125 mm and b) 22.3375 mm depth in water. Number of primary photons is 3.2×10^{10} . Dose values are in units of 10^{-4} Gy.

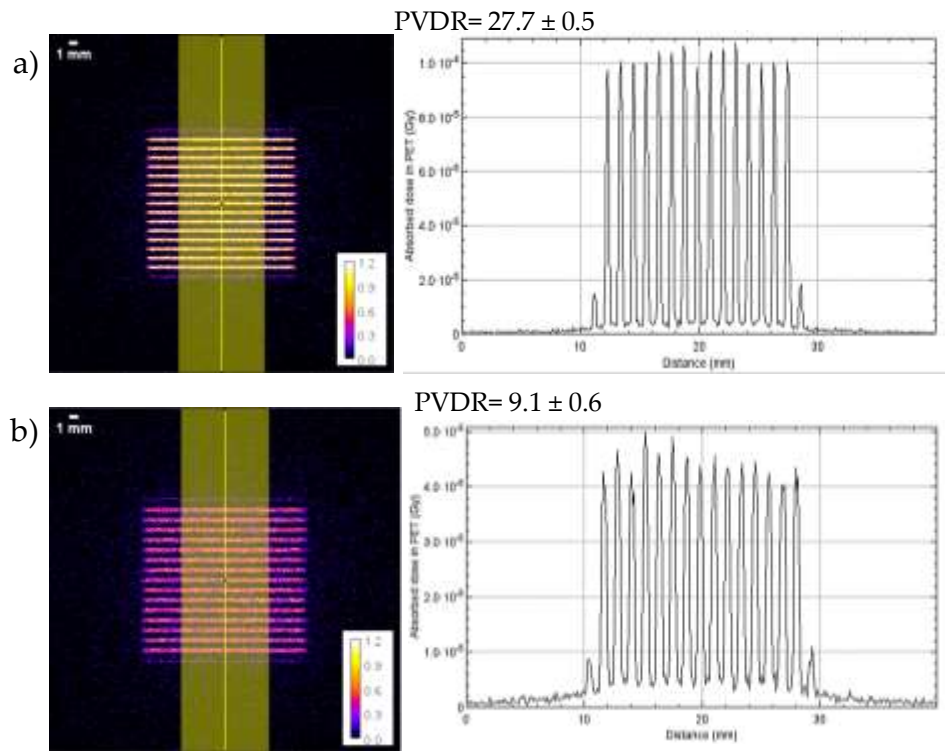


Figure 33: MBRT dose maps in PET (left) (40 mm x 40 mm) and corresponding line dose profiles (right) simulated with a 225 kVp, 0.3 mm Cu added filtration, X-ray beam with a focused multislit brass collimator (0.3 mm width aperture, 1 mm centre-to-centre distance, 40 mm thick) at a) 1.0125 mm and b) 22.3375 mm depth in water. Number of primary photons is 3.2×10^{10} . Dose values are in units of 10^{-4} Gy.

To obtain the PDD (Percentage Depth Dose) I simulated an open field irradiation of the same phantom as the previously simulation but changing the beam aperture to gain an irradiated area of $1 \times 1 \text{ cm}^2$, $2 \times 2 \text{ cm}^2$, and $3 \times 3 \text{ cm}^2$, using no collimator. The position of the phantom was identical to the one in the MBRT simulation with a brass collimator 4 cm thick, but in this case, I simply removed the MB collimator to obtain the open field irradiation. The dose was scored at a gafchromic PET film using an X-Ray beam source of 225 kV. Results are shown in Figure 34, 35 and 36, and the corresponding graphs are presented below.

I would determine the beam homogeneity in depth e the Percentage Depth Dose (PDD).

To calculate the PDD I opened the stack in ImageJ, I selected a ROI on the gafchromic film image, and used 'measure' to obtain the dose value in the ROI for each slice of the stack. Firstly, I plot the dose (Gy) versus the corresponding film number, and then I normalized the dose at the maximum to obtain the PDD shown in the graph. It had come to my attention that there was a high error of the dose in the PDD chart. Furthermore, due to the low statistic employed, the graphic representation of the dose profile showed a high fluctuation in the dose of the open part. Simultaneously, on the rising portion of the dose profile, corresponding to the beam opening, I noticed a double curve probably caused by the low pre collimator thickness (5 mm Pb) which passed part of the beam though the edges.

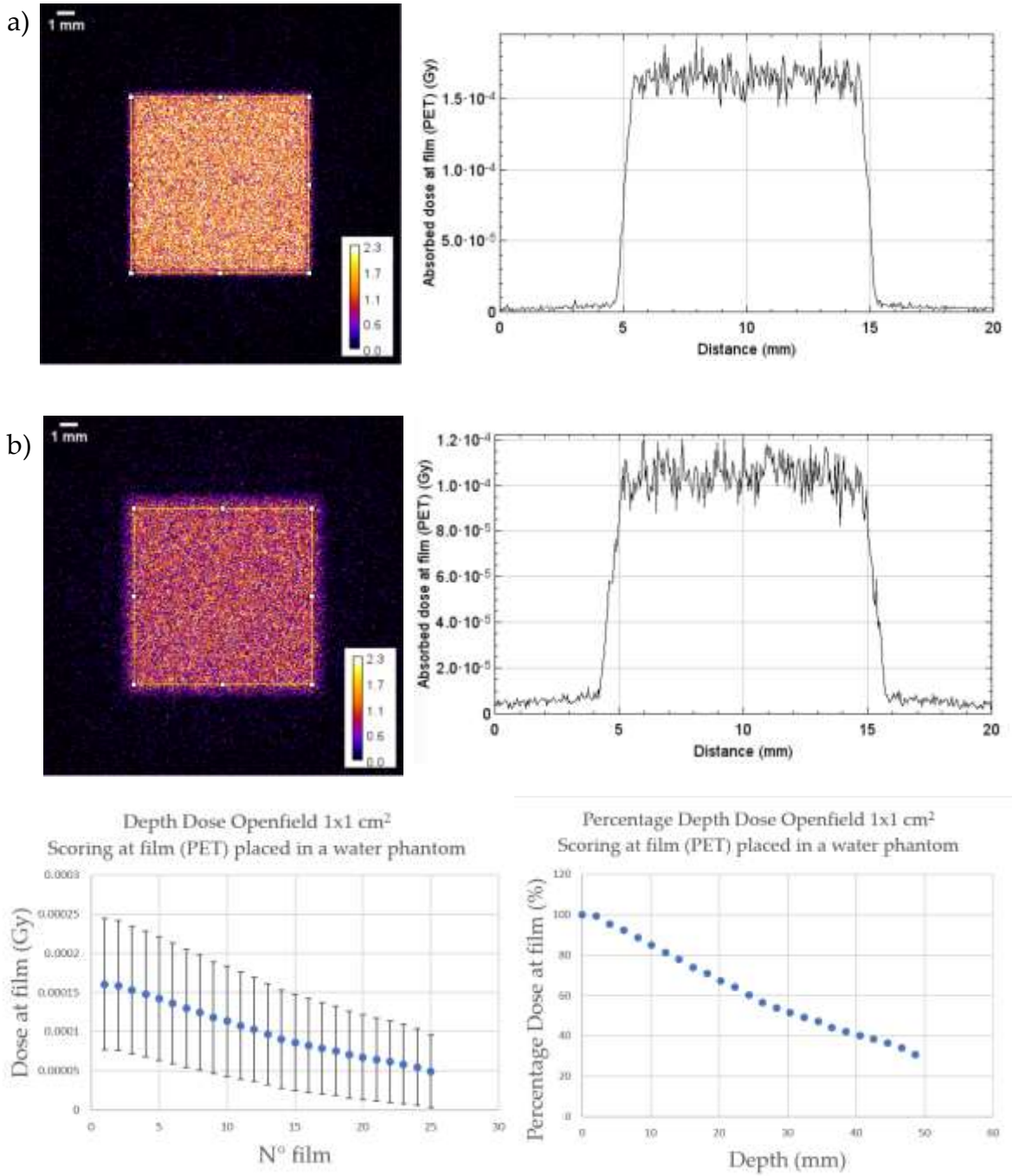


Figure 34: Open field 1x1 cm² dose maps in PET (left) (20 mm x 20 mm) and corresponding line dose profiles (right) simulated with a 225 kVp, 0.3 mm Cu added filtration, X-ray beam with no collimator at a) 0.0125 mm and b) 24 mm depth in water. Number of primary photons is 3.2×10^{10} . The selected ROI shown in the figure is the one used to obtain the mean pixel value. Dose values are in units of 10^{-4} Gy. Below the corresponding PDD graph.

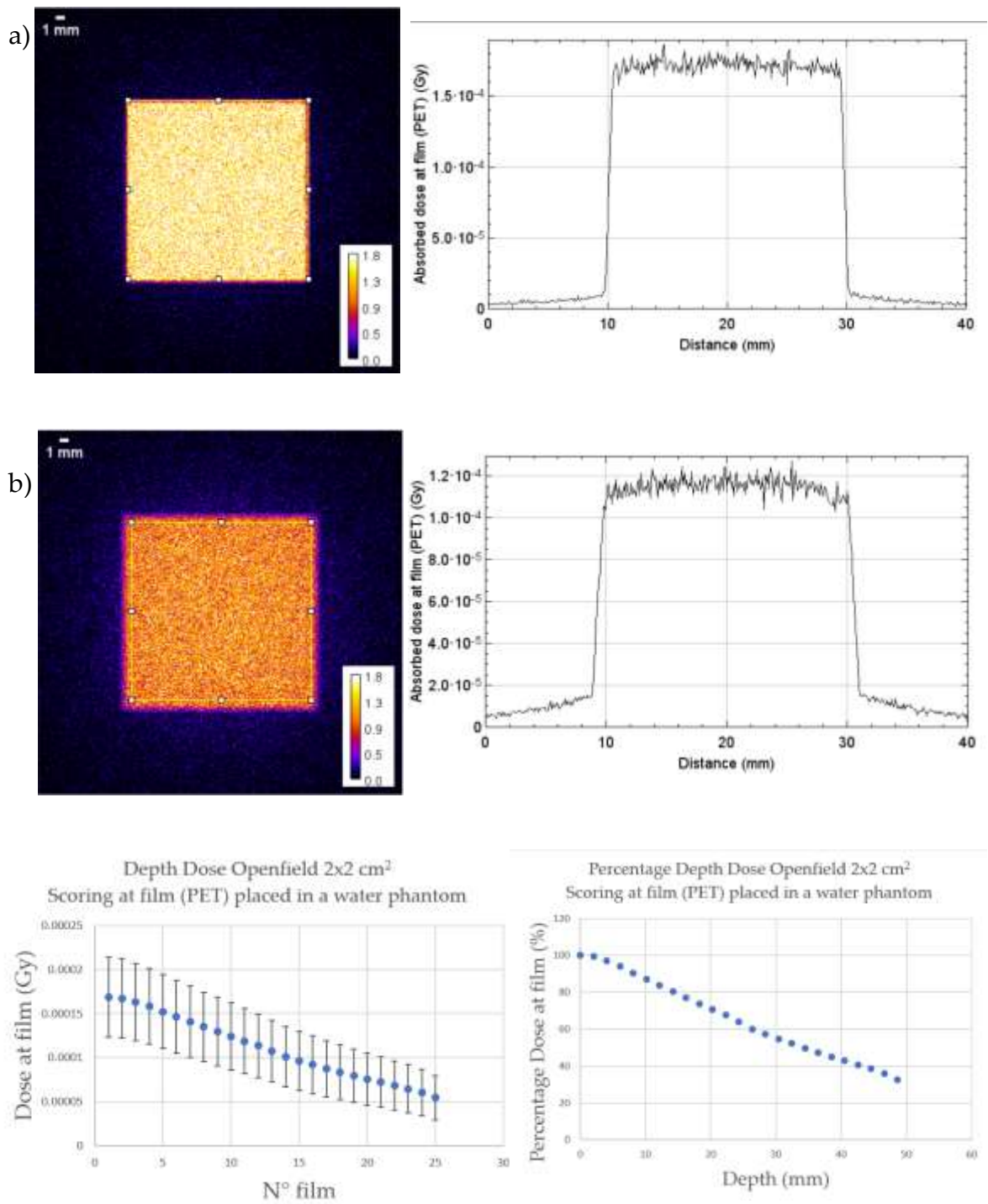


Figure 35: Open field $2 \times 2 \text{ cm}^2$ dose maps in PET (left) ($40 \text{ mm} \times 40 \text{ mm}$) and corresponding line dose profiles (right) simulated with a 225 kVp, 0.3 mm Cu added filtration, X-ray beam with no collimator at a) 0.0125 mm and b) 24 mm depth in water. Number of primary photons is 3.2×10^{10} . Dose values are in units of 10^{-4} Gy. The selected ROI shown in the figure is the one used to obtain the mean pixel value. Below the corresponding PDD graph.

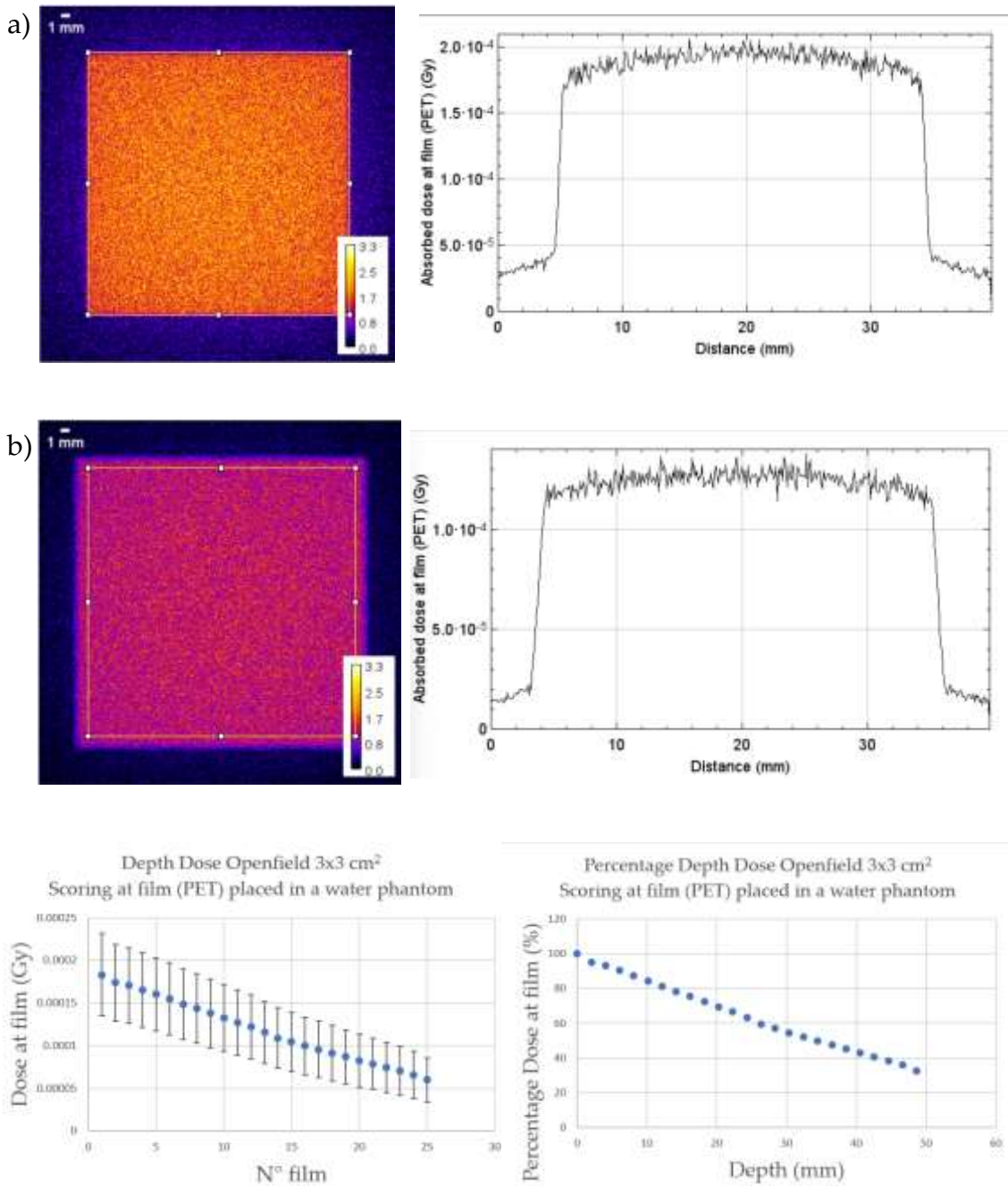


Figure 36: Open field 3x3 cm² dose maps in PET (left) (40 mm x 40 mm) and corresponding line dose profiles (right) simulated with a 225 kVp, 0.3 mm Cu added filtration, X-ray beam with no collimator at a) 0.0125 mm and b) 24 mm depth in water. Number of primary photons is 3.2x10¹⁰. Dose values are in units of 10⁻⁴ Gy. The selected ROI shown in the figure is the one used to obtain the mean pixel value. Below the corresponding PDD graph.

2.4 Rotational MBRT

Definitely, it was possible to improve the MBRT technique using different materials (i.e., brass) and patterns (different beamlets configuration) without losing efficiency. For this reason, I could explore a new MBRT irradiation mode that is able to improve the effectiveness of this technique, such as using a focused collimator able to rotate around the target to project the radiation beam only on the tumour. More specifically, by performing rotational irradiation from each angle it is possible to give the maximum dose to the centre (where the tumour can be found), since the contribution given by all the projections will be summed up here, and at the same time reduce the dose of $1/360^\circ$ to the healthy tissue. To confirm this theoretical idea, I simulated a 360° irradiation around a water phantom ($5 \times 5 \times 5 \text{ cm}^3$) using a X-Ray beam 225 kVp, 0.3 mm Cu filtration, source and as the previously presented simulations a brass focused collimator. Instead of using radio-chromic films placed in the phantom, I selected the command 'Depth Dose' in TOPAS which has a 3D dose map distribution output '.dat' format. The dose map obtained was then examined via Matlab program 'DoseMapRotational.m', which is shown below (Figure 37). In this program I converted the output simulation file '.dat' to a matrix and saved it as a stack in '.tif' format, called 'mappa3D_MBRT.tif', recalling the function 'saveasTIFF_LC' (Figure 38).

```
clear all
output_data=readmatrix("Dose_map_focused.csv");
a=500;
b=500;
c=500;
mappa_dose=cast(zeros(a,b,c),'single');
for i=1:size(output_data,1)
mappa_dose(output_data(i,1)+1,output_data(i,2)+1,output_data(i,3)+1)= output_data(i,4);
end
saveasTIFF_LC(mappa_dose, 'mappa3D_MBRT.tif',3,32);
```

Figure 37: Matlab code using to convert the output '.dat' file in a '.tif' file.

```

function saveasTIFF_LC(A, filename, sampleformat, bitspersample)
    t = Tiff(filename,'w');
    tagstruct.ImageLength = size(A,1);
    tagstruct.ImageWidth = size(A,2);
    tagstruct.SampleFormat = sampleformat;
    tagstruct.Photometric = Tiff.Photometric.MinIsBlack;
    tagstruct.BitsPerSample = bitspersample;
    tagstruct.SamplesPerPixel = 1;
    tagstruct.Compression = Tiff.Compression.None;
    tagstruct.PlanarConfiguration = Tiff.PlanarConfiguration.Chunky;
    for ii = 1:size(A,3)
        setTag(t, tagstruct);
        write(t, A(:,:,ii));
        writeDirectory(t);
    end
    close(t)
end

```

Figure 38: Matlab code of 'saveasTIFF_LC' function.

Afterwards, I opened the results via ImageJ using a macro (Figure 39) in which I created each projection rotating the coronal view of the stack by 1° at a time. Every single projection was summarised and converted in axial view.

```

open("C:/Users/ritac/OneDrive/Desktop/rotational_MBRT_focused/mappa3D_MBRT.tif");
selectWindow("mappa3D_MBRT.tif");
run("To CoronalTP", "input=[Axial (caudal-to-cephalic)]");
saveAs("Tiff", "C:/Users/ritac/OneDrive/Desktop/rotational_MBRT_focused/coronal_dosemap.tif");
selectWindow("mappa3D_MBRT.tif");
close();
selectWindow("coronal_dosemap.tif");
run("Duplicate...", "");
run("Rotate...", "angle=1 grid=1 interpolation=Bicubic stack");
imageCalculator("Add create 32-bit stack", "coronal_dosemap.tif", "coronal_dosemap-1.tif");
selectWindow("Result of coronal_dosemap.tif");
saveAs("Tiff", "C:/Users/ritac/OneDrive/Desktop/rotational_MBRT_focused/Result.tif");
close();
selectWindow("coronal_dosemap.tif");
close();
selectWindow("coronal_dosemap-1.tif");
close();
for (i=2; i<361; i++) {
    open("C:/Users/ritac/OneDrive/Desktop/rotational_MBRT_focused/coronal_dosemap.tif");
    run("Rotate...", "angle="+i+" grid=1 interpolation=Bicubic stack");
    open("C:/Users/ritac/OneDrive/Desktop/rotational_MBRT_focused/Result.tif");
    imageCalculator("Add create 32-bit stack", "coronal_dosemap.tif", "Result.tif");
    selectWindow("Result of coronal_dosemap.tif");
    saveAs("Tiff", "C:/Users/ritac/OneDrive/Desktop/rotational_MBRT_focused/Result.tif");
    close();
    close();
    close();
}

```

Figure 39: ImageJ macro used to summarize the MBRT simulation results and made the rotational MBRT simulation.

The results (Figure 40) show that the sagittal line dose profile preserves the MBRT pattern of the Peak-Valley which was previously observed. Additionally, the

dose at the peak is maintained and results to be higher than that the one obtained with a single view. The coronal line dose profile shows that the dose sums up at the centre and it is the double of the one of the peripheral regions, as it was expected. Thus, in this way it is possible to increase the dose to a possible tumour and at the same time sparing the healthy tissue in the peripheral area.

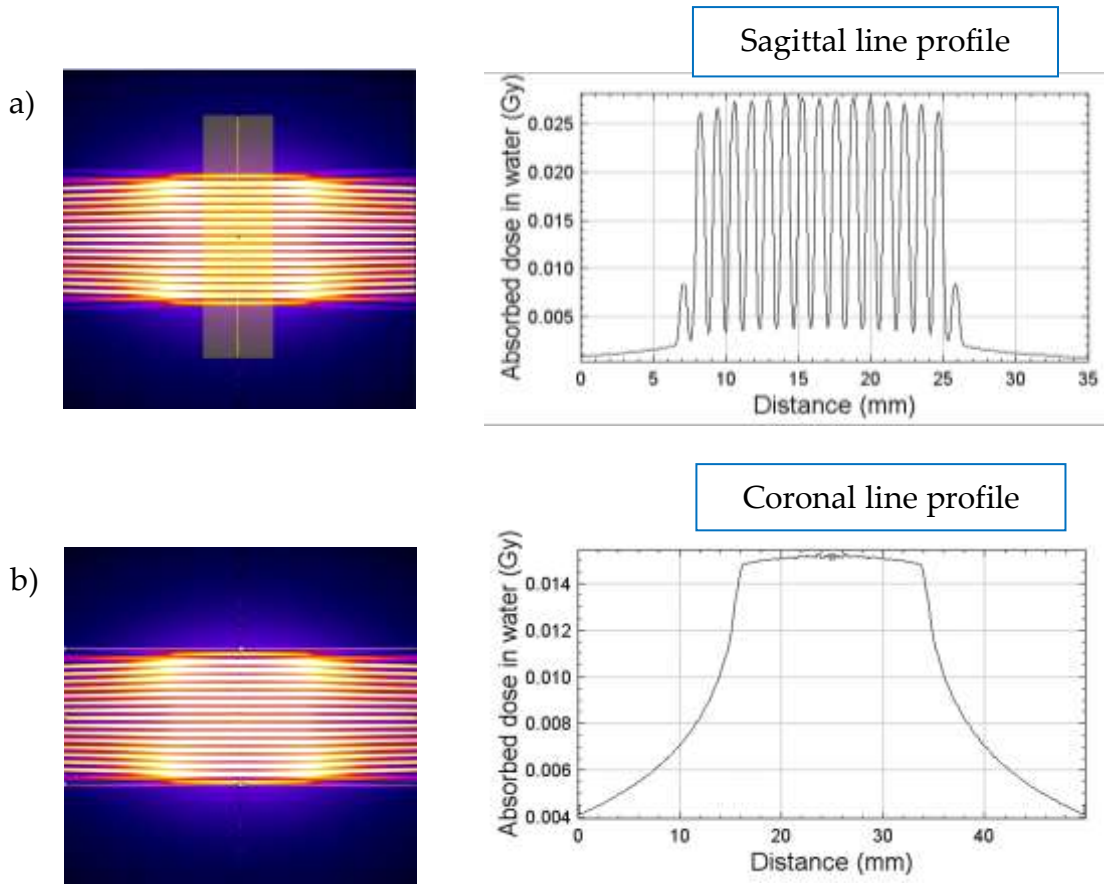


Figure 40: MBRT dose maps in PET (left) (20 mm x 20 mm) and corresponding line dose profiles (right) simulated with a 225 kVp, 0.3 mm Cu added filtration, X-ray beam with a focused multislit brass collimator (0.3 mm width aperture, 1 mm centre-to-centre distance, 40 mm thick) in a water phantom.

Chapter 3: Experimental validation

I validated the Monte Carlo simulations in chapter 2 through measurement carried out in the laboratory of Medical Physics at this Dept. of Physics, where there is an X-Ray tube operated at 150 kV, 0.5 mA. In paragraph 1 I describe the measurement set up and results, while in paragraph 2 I show the corresponding Monte Carlo simulation. To this purpose I fabricated a brass collimator 1 cm thick, in the mechanical shop of the Dept.

3.1 Measurement with 150 kVp source

The laboratory set up included a Hamamatsu 150 kV X-Ray tube as source, a brass collimator 1 cm thick, and Plexiglas phantom (Figure 41).

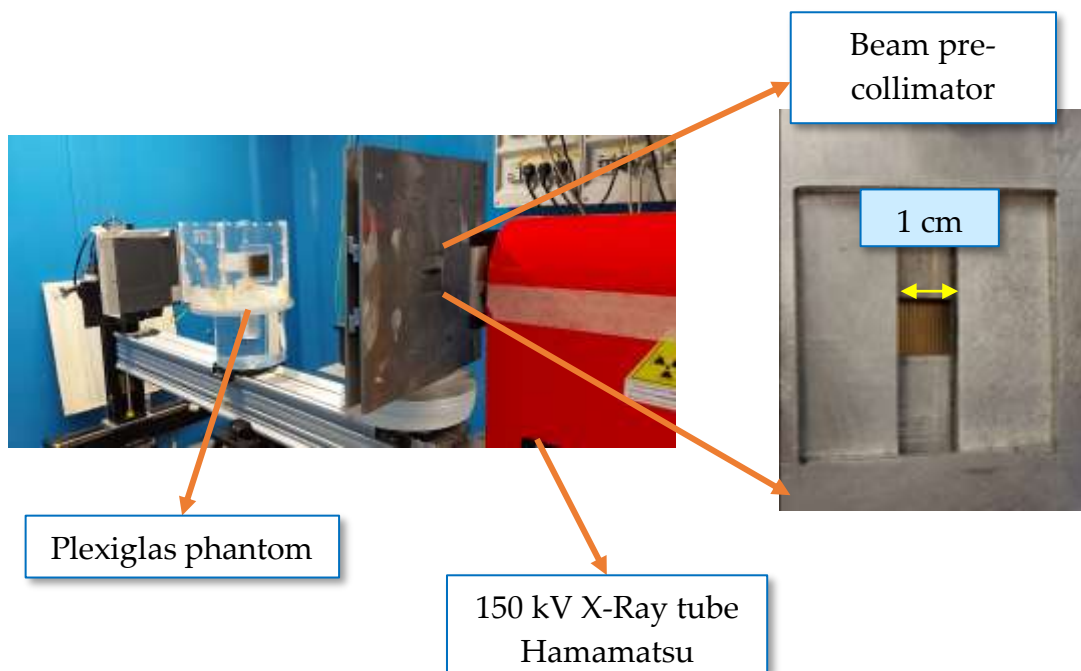


Figure 41: *Laboratory set up used to obtain experimental data.*

Hamamatsu 150 kV X-Ray tube L8121-03 is powered by a low power control unit and its anode is made of tungsten. It has an intrinsic filtration of 0.2 mm Beryllium (Be) and an additional one given by a filter of 1.54 mm Aluminium (Al) (99.9% pure) placed immediately at the exit of the tube, and the conic beam aperture is about 43° . Working at a constant current of $500 \mu\text{A}$, for voltages

varying between 40 kV and 150 kV (with a ripple in the range from 0.6 to 2.5%), the heat load tube curves, shown below (Figure 42), provide, for this operational range, a focal mode "large" and therefore a focal spot of 50 μm , which is 17mm from the Beryllium window.

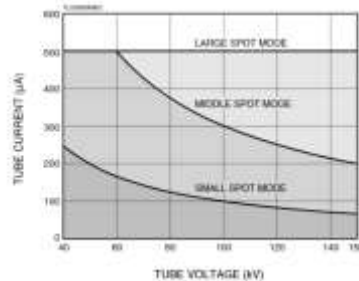


Figure 42: Heat load curves of Hamamatsu 150 kVp X-Ray tube.

The collimator was realized through the electro-discharge machining using brass material of 1 cm thick (Figure 43).

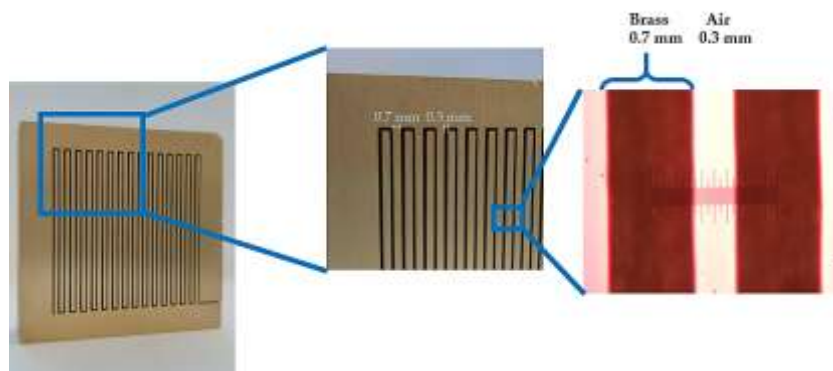


Figure 43: First sample of brass minibeam collimator, 10 mm thick, fabricated using electro-discharge machining.

The radio-chromic films used in this experiment are the XR-SP2 gafchromic films, the specifications of which are set out in Table 1 below. However, this type of films is not perfectly suitable for dose measurements, but only for geometric calibrations such as centring beams of X-ray tubes. These films are self-developing and are analysed using a LED scanner, so that the signal is studied in reflection. In this way, it is possible to obtain a continuous dose distribution. Figure 44 shows the scheme of the gafchromic composition.

Dose Range	Energy Range	Size	Active Layer Thickness
0.05 Rad to 10 Rads	20 KVp to 200 KVp	8"x10" or 10"x12"	25 microns

Table 1: XR-SP2 gafchromic facilities.

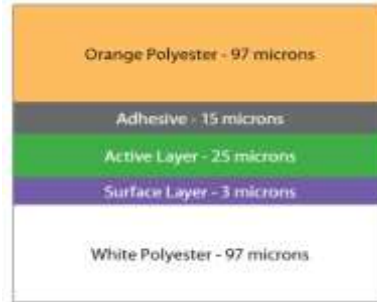


Figure 44: Structure of XR-SP2 gafchromic.

Particularly, the scanner used for the analysis of gafchromic films is the Epson v850pro flatbed scanner, which is equipped with a dual lens system that automatically selects the most suitable lens. It has an optical resolution of up to 4.800 dpi for scanning photographs and 6.400 dpi for scanning films through the appropriate media, which allows to obtain 48-bit RGB (*Red Green Blue*) images. Before proceeding with the actual measurement, it was necessary to determine the calibration curves that show the trend of the Air Kerma (K) as a function of the net difference in reflectance of the gafchromic films, pre- and post-exposure (net ΔR). Since for low doses this curve is almost flat, it was necessary to set the measurements, fixing the experimental points in terms of dose values. Here, I chose 8 points non-zero dose values (5-15-20-35-50-65-75-85 mGy). First, the entire gafchromic sheet was cut, to obtain smaller samples for the subsequent phase of exposure to X-rays. A shear stress was considered, which was propagated along an average thickness of 1 cm, in which the gafchromic response was evaluated. The selection of the area of interest during exposure had pass through the determination of an edge of 1 cm. From the entire film (25.4x30.48 cm²), 8 cut-outs (one for each fixed exposure dose level) of area 3x3 cm² were obtained, and for each of them 3 ROI were considered for analysis. Before

proceeding with the exposure of the film, the film itself was scanned for the determination of the average pre-exposure signal (in terms of *mean Pixel Value*) and, therefore, the subsequent evaluation (post-exposure) of the net reflectance difference (net ΔR). Here, I mention the net reflectance difference since radiation is not the only agent that induces the blackening of gafchromic films. Indeed, other factors, such as the interaction with air molecules, may be taken in consideration. Consequently, I only wished to highlight the contribution of ionizing radiation in the net difference. The characterization of the reflectance, in terms of blackening of the film, depends on the position of the same on the scanner; therefore, a frame was built to locate the gafchromic films on the scanning plate, always in the same position, so that the positional homogeneity in the response was guaranteed. I proceeded by installing the program Epson Scanner for the acquisition of the gafchromic film image; the mode of use of the application is not automatic but professional. It was possible to set the resolution of the image I wanted to obtain starting from the preliminary setting of the dpi (*dots per inch*): a too high dpi increases the noise while, on the contrary, a low dpi provokes a loss of resolution, so a balance had to be reached between the two opposite trends by setting a dpi value equal to 72. Once the image was obtained from the scanner in TIFF format³ (called "A_crop number_before") it was analysed with the free Java software, ImageJ. The program allows you to separate the initial scanned image with a depth of 48bit into its 16bit RGB components, *Red*, *Green* and *Blue*, which can then be analysed separately. Here, I performed a first qualitative analysis by adjusting the brightness and the contrast of the image and observing at the same time the possible presence of impurities caused by dust or cutting stress. The scanner presents a time-dependent variation in operation due to its progressive heating, a factor that introduces uncertainty on the

²dpi (*dots per inch*): density of graphic information that can be rendered by an output device (graphic [printer](#), [plotter](#), RIP, [screen](#)) or provided by an input device ([scanner](#) , [mouse](#)).

³ Tagged Image File Format (TIFF)

measurement of reflectance. For this reason, I chose to acquire 5 images for each of the 8 gafchromic clippings and discard the first two scans, assuming that after these measurements the scanner is in a good operational mode.

The gafchromic calibration curve, which showed the trend of the film response in terms of average pixel intensity (Pixel Value) as a function of radiation dose (mGy), was characterized in the three RGB channels but presented a greater sensitivity in the discrimination of low doses of exposure for the red channel, if compared to the blue and green channels. The trend of the expected calibration curve is polynomial but in a low dose range it is approximately linear, saturating for very high doses since once the maximum blackening is reached no more information can be obtained. After having scanned the gafchromic films, I proceeded with their exposure to X-Ray irradiation. In the system configuration for measurements, I placed the gafchromic film at the exit of the pre-collimator, irradiating an area of 1x1 cm².

Gafchromic films should be exposed to a known dose, establishing a certain distance from the source and positioning the ionization chamber, to measure the Air Kerma at that point. This was done in order to monitor the dose of film exposure during the measurement. However, before progressing to the measurement of the Air Kerma the chamber had to be positioned in the radiation cone of the tube, therefore, a centring was carried out by acquiring an image. Film exposures were made using the X-ray tube configured at 150 kV and 400 μ A with *tube load* 4 mAs. Once the 5 scans for each crop were acquired, 3 ROI of equal size (pixels) were selected to advance with the analysis. The analysis had to be repeated in the same conditions for each of the 8 gafchromic clippings, so the process was automated by implementing a macro for reading the samples in ImageJ on a suitable text file (Figure 45). Here, it is shown the macro implemented for the analysis of the pre-exposure film in the red RGB channel ("red_macro_before"):

```

for (i=1; i<13; i++) {
for(j=3; j<6; j++) {
open("C:/Users/ritac/OneDrive/Desktop/UNI/LAB FISICA MEDICA/gafchromici_before/A"+i+"_before_g3_00"+j+".tif");
selectwindow("A"+i+"_before_g3_00"+j+".tif");
run("split Channels");
close();
close();
makeRectangle(311, 334, 27, 40);
run("Measure");
makeRectangle(338, 334, 27, 40);
run("Measure");
makeRectangle(324, 374, 27, 40);
run("Measure");
selectwindow("C1-A"+i+"_before_g3_00"+j+".tif");
close();
}
}
saveAs("Results", "C:/Users/ritac/OneDrive/Desktop/UNI/LAB FISICA MEDICA/gafchromici_before/red/Results_red_before.csv");

```

Figure 45: ImageJ macro used to analyse the pre-exposure film in red channel.

The text file "macro rosso_before" was characterized by some specific commands that were necessary to proceed with the analysis of all the acquired images. "run("split channels")" allowed to separate the RGB channels and it was followed by a "close" command that needed to close the windows of the green and blue image. Two "for" cycles could be found next: the first one was needed to open each of the 3 acquisitions (because the first two were discarded to wait for the scanner's warm-up times), while the second one was required to open each scan of the 12 clippings. Finally, the obtained data were saved in an Excel file called "Results_red_before".

For each of the 3 ROIs of the individual gafchromic films (Figure 4) the values of the mean of the signal (Mean) were reported in the Excel files by averaging each signal of the same ROI on the 3 scans and the respective standard deviation (StdDev) obtained from ImageJ. I used the average of these values to obtain a unique value for each ROI. Therefore, in order to obtain the difference in reflectance (ΔR_i) for each ROI, the following relation was used:

$$\Delta R_i = \frac{(PV_{before} - PV_{after})}{2^{16}}$$

where PV_{before} and PV_{after} represent the average values calculated for each ROI considering scan number 3, 4, and 5, before and after exposure, respectively.

On the other hand, in order to obtain the error on ΔR_i I used the relation of the propagation of errors in the statistical mode:

$$\sigma_{\Delta R_i} = \sqrt{\frac{\sigma_{\langle ROI \rangle i \text{ before}}^2 + \sigma_{\langle ROI \rangle i \text{ after}}^2}{2^{16}}}$$

I proceeded by adding the values of the ΔR_i , each with the appropriate weights w_i :

$$w_i = \frac{1/\sigma_{\Delta R_i}^2}{1/\sigma_{\Delta R_1}^2 + 1/\sigma_{\Delta R_2}^2 + 1/\sigma_{\Delta R_3}^2}$$

Therefore:

$$\Delta R = \Delta R_1 w_1 + \Delta R_2 w_2 + \Delta R_3 w_3$$

Ultimately, $Net\Delta R$ is calculated as follows:

$$Net\Delta R = \Delta R - R_{control}$$

Where $R_{control}$ is the reflected ratio calculated for the unexposed film. The relative error was calculated with error propagation as follows:

$$\sigma(Net\Delta R) = \sqrt{\sigma_{\Delta R}^2 + \sigma_{R_{control}}^2}$$

The Table 2 of values obtained for the analysis of the red channel and the respective graphs are presented in Figure 46 below:

n gaf	ΔR	$\sigma\Delta R$	K (mGy)	$\sigma\Delta R(\%)$	σK
A1	0.312	0.002	65	0.63033	3.25
A2	0.277	0.003	50	0.952825	2.5
A3	0.345	0.003	85	0.945213	4.25
A4	0.146	0.002	15	1.435868	0.75
A5	0.166	0.002	20	1.147358	1
A6	0.054	0.002	5	3.807783	0.25
A7	0.235	0.003	35	1.295481	1.75
A8	0.328	0.003	75	0.775014	3.75

Table 2: Red channel analysis result for XR-SP2 gafchromic films.

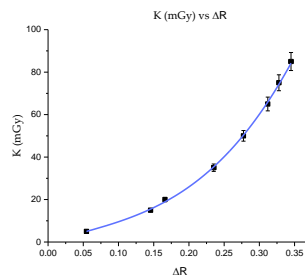


Figure 46: Calibration curve of XR-SP2 gafchromic films.

Subsequently, I proceeded with the exposure of gafchromics using the MB collimator at the output of the X-Ray tube. The laboratory set up consist of the Hamamatsu 150 kVp X-Ray tube, collimator housing, brass MB collimator, and a plexiglass phantom filled with water (Figure 47).

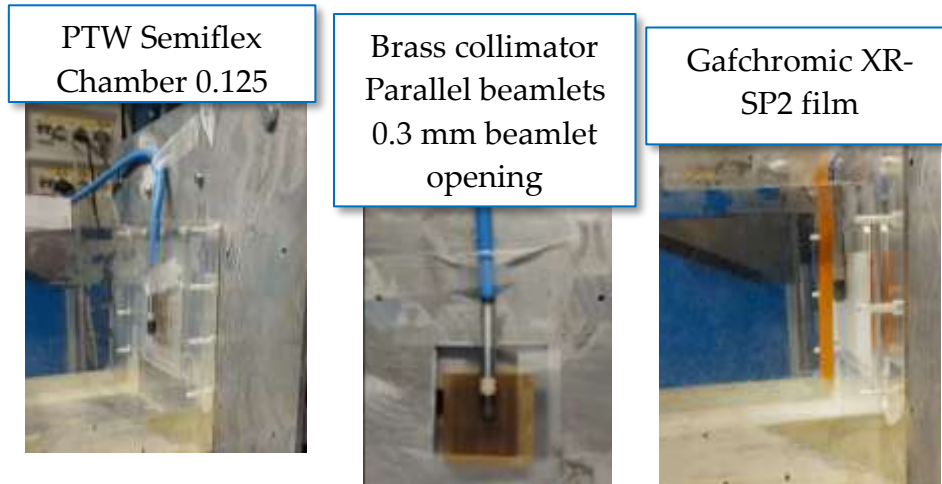


Figure 47: Laboratory set up used to irradiate the XR-SP2 gafchromic films with brass collimator 1 cm thick.

From the entire film ($25.4 \times 30.48 \text{ cm}^2$), 4 cut-outs (one for each fixed exposure dose level) of area $5 \times 10 \text{ cm}^2$ were got and named B1, B2, B3, and B4. Each gafchromic film were placed at different position, thus, I acquired the dose map at different depth in water or/and air. I exposed the gafchromic films at various dose value. Consequentially, each cut-out was scanned to acquire an image in TIFF format which was analysed via ImageJ. The acquisition procedure was the same as previously seen to acquire the gafchromic calibration curve, PI changed only the dpi value to 300. Indeed, the calibration curve allowed for the conversion of the image's pixel value to dose of the irradiated gafchromic film images. Since I applied the same procedure to all of the gafchromic film images to calibrate them, I implemented an ImageJ macro (Figure 48).

```

for (i=1; i<6; i++) {
for(j=3; j<6; j++) {

open("C:/Users/ritac/OneDrive/Desktop/scansione gaf/gaf_5x10_after_bis/B"+i+"_after_00"+j+"_crop.tif");
open("C:/Users/ritac/OneDrive/Desktop/scansione gaf/gaf_5x10_before_bis/B"+i+"_before_00"+j+"_crop.tif");
selectWindow("B"+i+"_before_00"+j+"_crop.tif");
run("Split Channels");
close();
close();
selectWindow("B"+i+"_after_00"+j+"_crop.tif");
run("Split Channels");
close();
close();
imageCalculator("Subtract create 32-bit", "C1-B"+i+"_before_00"+j+"_crop.tif", "C1-B"+i+"_after_00"+j+"_crop.tif");
selectWindow("Result of C1-B"+i+"_before_00"+j+"_crop.tif");
run("Divide...", "value=65536");
saveAs("Tiff", "C:/Users/ritac/OneDrive/Desktop/scansione gaf/gaf_5x10_after_bis/R_B"+i+"_00"+j+".tif");
selectWindow("C1-B"+i+"_before_00"+j+"_crop.tif");
close();
selectWindow("C1-B"+i+"_after_00"+j+"_crop.tif");
close();
selectWindow("R_B"+i+"_00"+j+".tif");
imageCalculator("Multiply create 32-bit", "R_B"+i+"_00"+j+".tif", "R_B"+i+"_00"+j+".tif");
selectWindow("Result of R_B"+i+"_00"+j+".tif");
rename("R2");
imageCalculator("Multiply create 32-bit", "R2", "R_B"+i+"_00"+j+".tif");
selectWindow("Result of R2");
rename("R3");
selectWindow("R_B"+i+"_00"+j+".tif");
run("Multiply...", "value=97.99731");
selectWindow("R2");
run("Multiply...", "value=-204.19892");
selectWindow("R3");
run("Multiply...", "value=1821.03713");
imageCalculator("Add create 32-bit", "R2", "R_B"+i+"_00"+j+".tif");
selectWindow("Result of R2");
imageCalculator("Add create 32-bit", "R3", "Result of R2");
selectWindow("Result of R3");
run("Subtract...", "value=0.03302");
selectWindow("R3");
close();
selectWindow("R_B"+i+"_00"+j+".tif");
close();
selectWindow("R2");
close();
selectWindow("Result of R2");
close();
selectWindow("Result of R3");
saveAs("Tiff", "C:/Users/ritac/OneDrive/Desktop/scansione gaf/B"+i+"_after_00"+j+"_calib.tif");
close();
}
}

```

Figure 48: *ImageJ* macro used to calibrate the exposed gafchromic films with MB collimator.

The calibrated gafchromic films were achieved thanks to the *ImageJ* macro and the results are shown below (Figure 49, 50 and 51). From the obtained line profile, the PVDR was calculated at the central peak and the fluctuation was estimated considering the variation of the peaks immediately on the right and left. I evidenced in the line profile (Figure 49) that the typical MB pattern was maintained, the peaks are well distinguished from each other both on the surface and in depth. Due to the beam attenuation, as I expected there was a decrease dose in depth that at the central peak goes from 60 to 40 mGy. It was also possible to highlight a decreasing trend at the edges of the intensity of the peaks and valley both and this phenomenon was caused by the beam divergence, it was also maintained in depth.

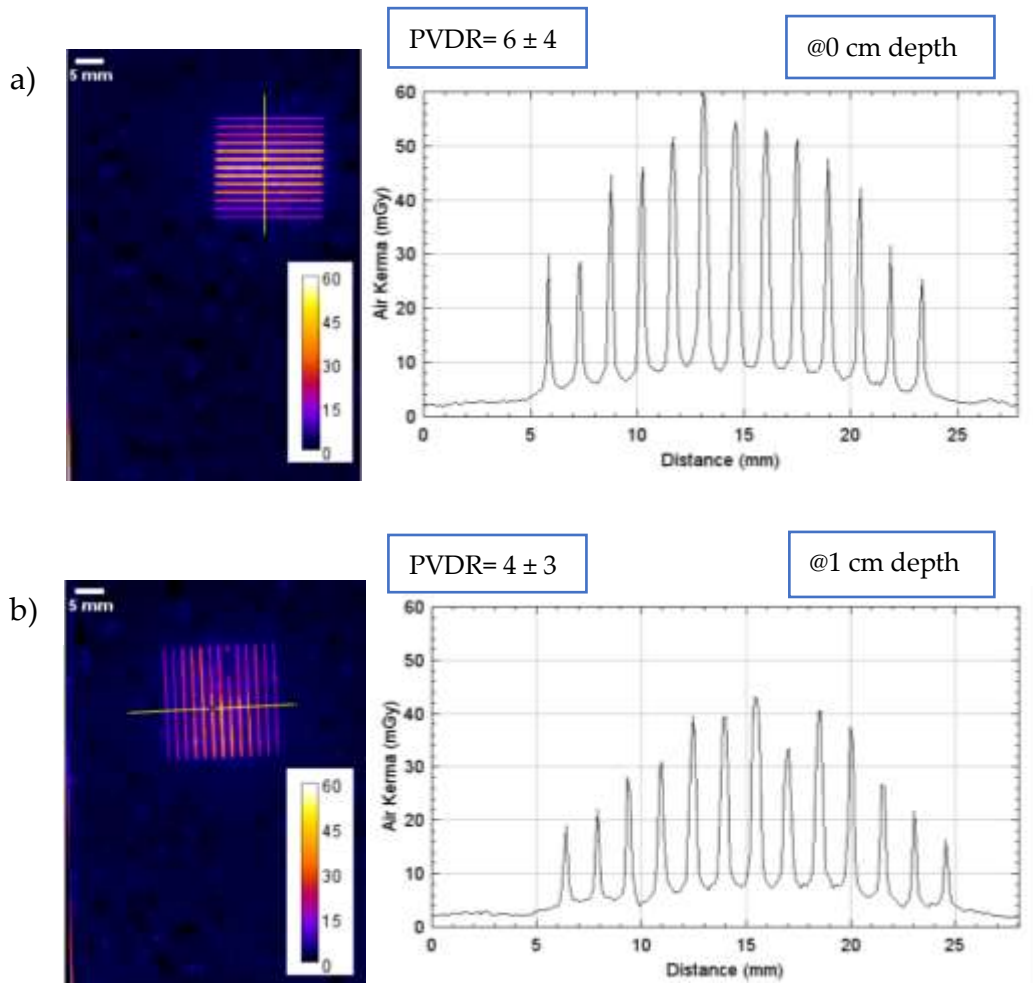


Figure 49: MBRT dose maps at gafchromic film B1 (left) and corresponding line dose profiles (right) simulated with a 150 kV, 0.2 mm Beryllium (Be) and 1.54 mm Al added filtration, X-ray beam with a multislit brass collimator (0.3 mm width aperture, 1 mm centre-to-centre distance, 10 mm thick) at a) 0 cm and b) 1 cm depth in water. Dose values are in units of mGy.

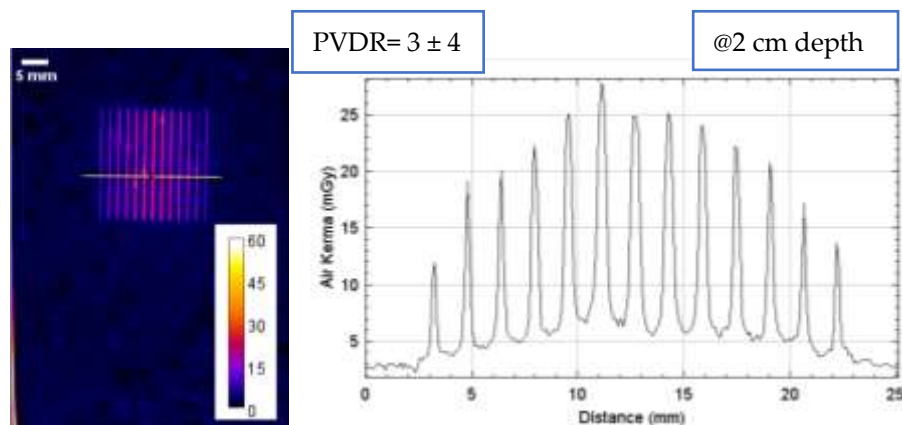


Figure 50: MBRT dose maps at gafchromic film B2 (left) and corresponding line dose profiles (right) simulated with a 150 kV, 0.2 mm Beryllium (Be) and 1.54 mm Al added filtration, X-ray beam with a multislit brass collimator (0.3 mm width aperture, 1 mm centre-to-centre distance, 10 mm thick) at 2 cm depth in water. Dose values are in units of mGy.

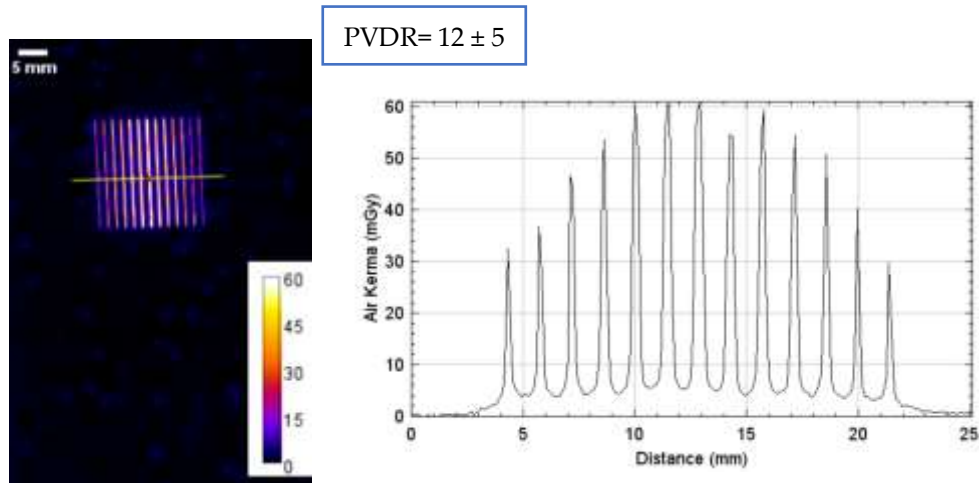


Figure 51: MBRT dose maps at gafchromic film B4 (left) and corresponding line dose profiles (right) simulated with a 150 kV, 0.2 mm Beryllium (Be) and 1.54 mm Al added filtration, X-ray beam with a multislit brass collimator (0.3 mm width aperture, 1 mm centre-to-centre distance, 10 mm thick) at collimator surface in air. Dose values are in units of mGy.

3.2 Simulation with 150 kVp source

I carried out a simulation, with features which emulated partially the laboratory set up, to test the adhesion with experimental results. In the simulation code I set as source the Hamamatsu 150 kVp spectrum obtained via TASMICS, then at 24.3 cm from the source was located the collimator housing in which I placed the simulated the multislit brass collimator 1 cm thick (0.3 mm width aperture, 1 mm centre-to-centre distance). The collimator housing was simulated with no pre collimator so all the gafchromic films placed were irradiated. At the collimator output surface, I placed a plexiglass phantom (15x15x15 cm³) filled with water simulated as a 'TsBox' (14x14x14 cm³) in which were located simulated gafchromic films (PET) 2x2 cm² (Figure 53). X-Ray source generated a beam with angular amplitude of 40 deg and 3.2×10^{10} number of primary photons.

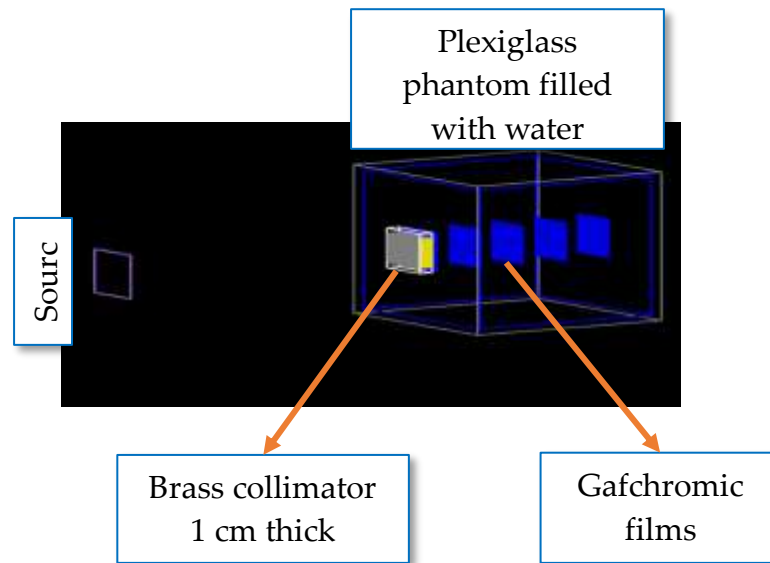


Figure 52: *Traversal view of water phantom (14x14x14 cm³) in blue placed in a plexiglass box (15x15x15 cm³) in grey, collimator housing in white.*

The gafchromic films were placed 2.5 cm apart in water phantom to analyse the beam widening and the deposited dose variation in depth. The simulation results are shown below (Figure 54).

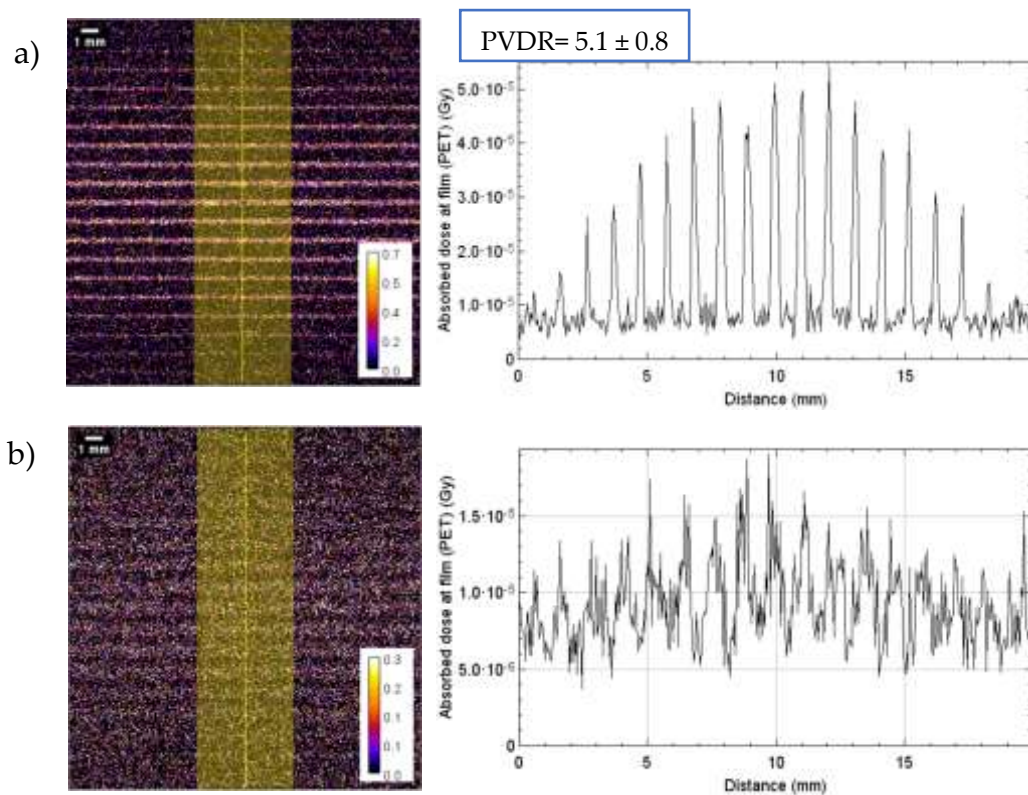


Figure 53: *MBRT dose maps in PET (left) (20 mm x 20 mm) and corresponding line dose profiles (right) simulated with a 150 kVp, 0.2 mm Beryllium (Be) and 1.54 mm Al added filtration, X-ray beam with multislit brass collimator (0.3 mm width aperture, 1 mm centre-to-centre distance, 10 mm thick) at a) 0.125 mm and b) 25 mm depth in water. Number of primary photons is 3.2×10^{10} . Dose values are in units of 10^{-4} Gy.*

The simulation results are different from the experimental one due to different issues. First at all, the simulated doses are in the order of dozens of μGy while the experimental doses are in the order of tens of mGy and this affected the fluctuation as seen in Figure 53, in fact the fluctuation still very high. The simulation results do not appreciate the effect described above in Section 3.1, i.e. the decrease at the edge of the input value, and this may be caused by the incompleteness description of the entire laboratory measurement system geometry in the MC simulation.

Conclusions

The most common method of treating cancer today is conventional X-ray radiation therapy. Conventional single-beam radiotherapy may cause an increase in neurotoxicity to tissues adjacent to the irradiated tumour, this remain a major problem. The collective aim of the scientific community is to find and study possible alternative ways to treat all cancers, in particular those that are radioresistant or that are in proximity to radiosensitive organs to reduce as much as possible neurotoxicity and increase the saving of healthy tissue.

The purpose of this thesis is to verify, through Monte Carlo simulations via TOPAS (Geant4 toolkit), the validity of the spatially fractionated beam radiotherapy technique, MBRT. The simulations in Chapter 2 are part of a larger project approved by the PNRR, "Developing and Optimizing X-Rays mini-beam Radiotherapy", promoted by the San Raffaele Hospital (HSR), Milan, in collaboration with the Azienda Ospedaliera Universitaria Federico II (AOU) and Università Federico II OF Naples, through which I also want to test new materials for the realization of MB collimator. Typically, the results obtained by simulations, even with the brass collimator, verify positive performance of the MB technique that is manifested in a good PVDR. Nevertheless, the number of photons used for the simulation (3.2×10^{10}) turned out to be a great limitation of TOPAS simulations, that manifests itself in a poor statistic of the results. The future goal will be to increase the number of events to increase statistics and thus improve dose estimation.

It was not possible to carry out the experimental measurements at the San Raffaele Hospital in Milan because the project "Developing and Optimizing X-Rays mini-beam Radiotherapy" formally started on 22 May 2023 but the funds for the start of the experiment have not yet been operational. Therefore, the experimental measurements were carried out at the laboratory of the Università Federico II of Naples and this has determined some limitations with respect to

the results obtained. The experimental results in Chapter 3 verify the possibility of implementing the MBRT using the conventional X-Ray tube. The dose in our experiment were obtained by taking a long exposure time due to the low maximum voltage of the Hamamatsu X-Ray tube (150 kV).

Ultimately, the research will continue to experiment with the MB technique from which good results are currently being obtained in the preclinical phase as seen in the literature existing in Chapter 1.

References

- [1] F. A. Dilmanian et al. Tissue-sparing effect of x-ray microplanar beams particularly in the CNS: Is a bystander effect involved?. *Exp. Hematol.* 2007;35(4 Suppl 1):69-77.
- [2] Y. Prezado et al. Transfer of Minibeam Radiation Therapy into a cost-effective equipment for radiobiological studies: a proof of concept. *Sci. Rep.* 2017;7(1):17295.
- [3] L. S. L. Price et al. Minibeam radiation therapy enhanced tumor delivery of PEGylated liposomal doxorubicin in a triple-negative breast cancer mouse model. *Ther. Adv. Med. Oncol.* 2021;13:1-14.
- [4] M. Sotiropoulos et al. X-rays minibeam radiation therapy at a conventional irradiator: Pilot evaluation in F98-glioma bearing rats and dose calculations in a human phantom. *Clin. Transl. Radiat. Oncol.* 2021;27:44-49.
- [5] K. M. Kraus et al. Treatment Planning Study for Microbeam Radiotherapy Using Clinical Patient Data., *Cancers (Basel)* 2022;14(3):685
- [6] Serduc R. et al. In vivo two photon microscopy study of short-term effects of microbeam irradiation on normal mouse brain microvasculature. *Int. J. Radiat. Oncol. Biol. Phys.* 2006;64(5):1519-27.
- [7] Bouchet A. et al. Effects of microbeam radiation therapy on normal and tumoral blood vessels. *Phys. Med.* 2015;31(6):634-41.
- [8] J. Spiga. Monte Carlo simulation of dose distributions for synchrotron Microbeam Radiation Therapy. PhD thesis, 2005
- [8] Bouchet A. et al. Preferential effect of synchrotron microbeam radiation therapy on intracerebral gliosarcoma vascular networks. *Int. J. Radiat. Oncol. Biol. Phys.* 2010;78(5):1503-12.
- [10] Bouchet A. et al. Synchrotron microbeam radiation therapy induces hypoxia in intracerebral gliosarcoma but not in the normal brain *Radiother. Oncol.* 2013;108(1):143-8.

- [11] C. Peucelle et al. Proton minibeam radiation therapy: Experimental dosimetry evaluation. *Med. Phys.* 2015;42(12):7108-13.
- [12] A. Espinosa-Rodriguez et al. Design of an X-ray irradiator based on a standard imaging X-ray tube with FLASH dose-rate capabilities for preclinical research. *Radiat. Phys. Chem.* 2023;206:110760.
- [13] J.D. Wilson et al. Ultra-high dose rate (FLASH) radiotherapy: silver bullet or fool's gold? *Front. Oncol.* 2020;9:1563.
- [14] Q. Zhang et al. Flash investigations using protons: design of delivery system, preclinical setup and confirmation of flash effect with protons in animal systems. *Radiat. Res.* 2020;194(6):656-664.
- [15] <https://www.geant4.org/news/2022-12-09-release11-1>
- [16] B. Faddegon et al. The TOPAS tool for particle simulation, a Monte Carlo simulation tool for physics, biology and clinical research. *Phys. Med.* 2020;72:114-121.
- [17] H. Paganetti H. Range uncertainties in proton therapy and the role of Monte Carlo simulations. *Phys. Med. Biol.* 2012;57(11):R99-117.
- [18] J. Perl et al. TOPAS: An innovative proton Monte Carlo platform for research and clinical applications. *Med. Phys.* 2012;39(11):6818-37.
- [19] J. Schuemann et al. TOPAS-nBio: An Extension to the TOPAS Simulation Toolkit for Cellular and Sub-cellular Radiobiology. *Radiat. Res.* 2019;191(2):125-138.

Acknowledgments

I would like to thank Prof. Russo, my thesis supervisor and guide, who has carefully supported my work.

I would like to thank my parents who have always supported me in all my choices.

I would like to thank those who have proved to be a true friend, shoulder, and conscience.

I would like to thank those who with a caress or a word of comfort took care of me.

I would like to thank those who have recently entered my life because it has made me appreciate the value of the unexpected.

I would like to also thank those who left because they taught me that nothing is forever.

I would like to thank those who believed in me from the beginning to the end.

I would like to thank those who love me and have truly loved me.